3D Shape Tokenization

Jen-Hao Rick Chang, Yuyang Wang, Miguel Angel Bautista Martin Jiatao Gu, Josh Susskind, Oncel Tuzel Apple

https://machinelearning.apple.com/research/3d-shape-tokenization

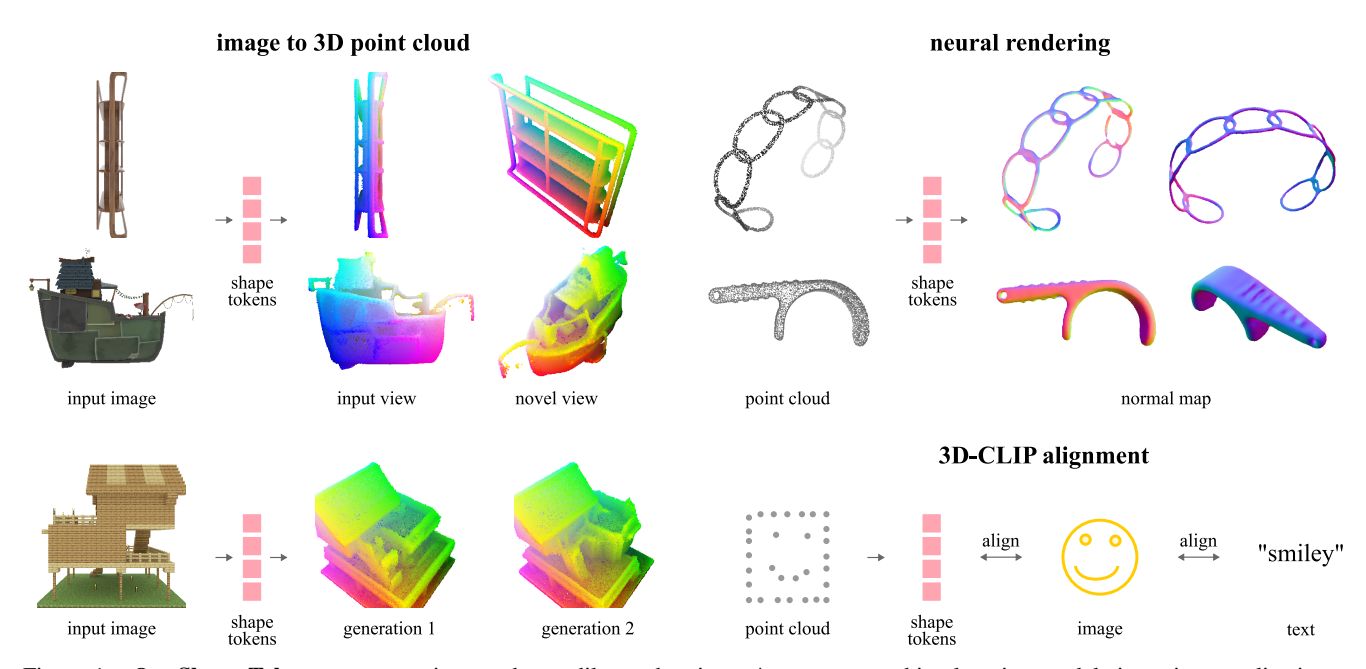


Figure 1. Our **Shape Tokens** representation can be readily used as input / output to machine learning models in various applications, including single-image-to-3D (left), neural rendering of normal maps (top right) and 3D-CLIP alignment (bottom right). The resulting models achieve strong performance compared to baselines for individual tasks. Mesh credits [3, 5, 6, 53, 66].

Abstract

We introduce **Shape Tokens**, a 3D representation that is continuous, compact, and easy to incorporate into machine learning models. Shape Tokens act as conditioning vectors that represent shape information in a 3D flow-matching model. The flow-matching model is trained to approximate probability density functions corresponding to delta functions concentrated on the surfaces of shapes in 3D. By attaching Shape Tokens to various machine learning models, we can generate new shapes, convert images to 3D, align 3D shapes with text and images, and render shapes directly at variable, user specified, resolution. Moreover, Shape Tokens enable a systematic analysis of geometric properties such as normal, density, and deformation field. Across all tasks and experiments, utilizing Shape Tokens demonstrate strong performance compared to existing baselines.

1. Introduction

How should 3D shapes be represented in learning systems? There are many available options: voxels [21, 39, 47], meshes [57, 70], point clouds [41, 64, 73, 85], (un-)signed distance fields [18, 46, 56], radiance/occupancy fields [54, 55, 61, 80], 3D Gaussian splats [38, 40], etc. In a typical setting, the choice of representation is determined by the downstream task of interest. For example, in graphics or rendering scenarios one may choose a mesh or a 3D Gaussian representation [38]. For scientific or physics simulation settings, continuous representations like fields might be able to encode fine-grained information [9, 30]. Yet, there seems to be no clear consensus on what constitutes a good representation for 3D shapes when training machine learning models. Most machine learning models require continuous and compact representations due to computation and memory constraints. Point-like representations are often chosen

due to their continuous nature and compatibility with recent architectures like transfomers [50, 85, 87]. However, tens and thousands of points are usually required to represent 3D shapes in high fidelity, making point clouds difficult to use in large systems.

Our hypothesis is that one can learn a continuous and compact representation of 3D shapes that encodes useful information for many different machine learning downstream tasks. In particular, we treat shapes as probability density functions in 3D space and use a flow matching generative model to learn representations of these densities by training on samples of each density function (*i.e.*, points sampled on surfaces of the shape). We call our representation **Shape Tokens** (**ST**) and it offers several desirable properties:

- ST are continuous and compact. Instead of representing a scene with a discrete mesh or tens of thousands of points, they represent diverse shapes with 1,024 continuous vectors of 16 dimensions, making it an efficient representation for downstream machine learning tasks.
- 2. Our approach makes minimal assumptions about the underlying structure of 3D shapes. We only assume that we can sample independent and identically distributed (i.i.d.) points from the surface of 3D shapes (i.e., obtaining point clouds from 3D objects). This is distinct from most 3D representations like signed distance functions (which assume water-tight shapes) and 3D Gaussians (which assume volumetric rendering).
- 3. At training time our method only requires point clouds. This is different from existing neural 3D representations that often require meshes or signed distance functions during training (*e.g.*, [88, 89]). This requirement significantly simplifies our training pipeline and enables us to scale our training set easily, as most meshes in large-scale dataset like Objaverse [20] are not watertight and are difficult to process.
- 4. Notably, ST enable systematic analysis of shapes, including surface normal estimation, denoising, and deformation between shapes (see Section 4.2).

We empirically demonstrate the effectiveness of our representation on a range of downstream tasks. First, we tackle 3D generation problems by learning an unconditional flow-matching model on ShapeNet [12] and an image-conditioned flow-matching model on Objaverse (see Section 5.1). Second, we showcase zero-shot text classification of 3D shapes by learning a Multi-Layer Perceptron (MLP) that aligns ST to image and text CLIP embedding [44] (see Section 5.2). Third, we showcase a graphics use case (ray-surface interaction estimation), by learning a neural network that takes a ray and ST as input and outputs intersection point and its normal (see Section 5.3). In all these tasks, we achieve competitive performance as baselines designed

for the specific tasks.

Finally, we found that a significant challenge holding back progress is the lack of readily available code and pretrained models from existing neural 3D representation methods trained on extensive datasets such as Objaverse (e.g., [88]). To address this issue and facilitate the advancement of future works, we will make a public release of pretrained shape tokenizers, image-conditioned latent flow-matching models, the 3D-CLIP model, our data rendering pipeline, and our full training code.

2. Related work

The field of 3D representation, generation, and classification is vast. We focus on discussing literature most relevant to our work — generative models of 3D representations. For an overview of 3D representations as a whole, we refer reader to [76].

There are several approach that learn latent representations and generative models of 3D shapes. MeshGPT [70] and MeshXL [17] learn auto-encoder of triangles and auto-regressive models to produce sequences of triangles. XCube [65] learns latent representations for occupancy grids of individual resolutions. 3DShape2VecSet [86], Michelangelo [90], Direct3D [79], and Clay [88] encode surfaces by learning to estimate occupancy at xyz locations. During training, these methods require meshes and extensive pre-processing and filtering to ensure the meshes are watertight, well-discretized (not too many triangles), or UV-mapped. In the point cloud domain, both Point-E [58] and LION [77] learn generative models of point sets of a fixed cardinality, i.e., they learn the joint distribution of a fixed number of points, i.e., $p(x_1, \ldots, x_k)$. Despite its permutation-invariance, it is a much higher dimensional function compared to our 3-dimensional distribution, which allows us to use compact latent to achieve similar reconstruction quality. Closely related to our approach are Luo and Hu [51] and PointFlow [85], which also consider 3D shapes as 3D probability density functions and use a generative model (diffusion model and continuous normalizing flow, respectively) to model the distributions. In comparison, we utilize flow matching and scale up our training from ShapeNet to Objaverse. Moreover, we demonstrate connections between the predicted velocity field in flow matching and geometric properties like surface normal and deformation fields, and we show that the learned 3D representation is useful beyond generative modeling (e.g., zero-shot classification and neural rendering).

Another interesting line of work utilizes images and differentiable rendering to supervise the estimation of 3D representations [28, 31, 42, 45, 63, 75, 81, 82]. The focus of these works are the realism of the rendered images — 3D representations and their distributions are not directly supervised or modeled, and thus are out of scope for this paper.

¹Note that "token" commonly denotes a discrete set of symbols in language models. Shape Tokens refer to a set of real-valued vectors.

3. Preliminary

We provide a preliminary overview of Flow Matching. Flow matching generative models [43, 52] learn to reverse a time-dependent process that turns data samples $x \sim p(x)$ into noise $\epsilon \sim e(\epsilon)$:

$$x_t = \alpha_t x + \sigma_t \epsilon, \tag{1}$$

where $t \in [0,1]$, x and $\epsilon \in \mathbb{R}^d$, α_t is an increasing function of t and σ_t is a decreasing function of t, and $p_0(x) \equiv e(x)$ is the distribution of noise and $p_1(x) \approx p(x)$ is the data distribution. The marginal probability distribution $p_t(x)$ is equivalent to the distribution of the probability flow Ordinary Differential Equation (ODE) of the following velocity field [52]:

$$\dot{x_t} = \frac{\mathrm{d}x_t}{\mathrm{d}t} = v_\theta(x;t),\tag{2}$$

where $v_{\theta}(x;t)$ can be learned by minimizing the loss

$$\mathcal{L}(\theta) = \int_0^1 \mathbb{E}\left[\|v_{\theta}(x_t; t) - \dot{\alpha}_t x_1 - \dot{\sigma}_t \epsilon\|^2 \right] dt.$$
 (3)

In practice, the integrations of time and the expectation are approximated by Monte Carlo methods, allowing simple implementations. Under this formulation, samples of $p_1(x)$ are generated by integrating the ODE (Eq. (2)) from t=0 to t=1. Note that the formulation allows flexible choices of $e(\epsilon)$, α_t , and σ_t , which we utilize in our paper, for more details we refer readers to [43, 52].

4. Method

We consider a 3D shape S as a probability density function $p_{\mathcal{S}}(x): \mathbb{R}^3 \to [0, \infty)$, where $x \in \mathbb{R}^3$ is a 3D location (i.e., $(xyz)^2$. A set of i.i.d. samples of $p_S(x)$ creates a point cloud, $\mathcal{X} = \{x_1, \dots, x_n\}$. Our goal is to fit $p_{\mathcal{S}}(x)$ with a conditional flow matching model $v_{\theta}(x; s, t) : \mathbb{R}^3 \to \mathbb{R}^3$, where $t \in [0,1]$ is the flow matching time, $s \in \mathbb{R}^{k \times d}$ are k ST representing the shape S, and θ is the parameters of a neural network v. The ST s are outputs of a tokenizer $\mu_{\theta}(\mathcal{S})$, which is jointly learned with the flow matching model to embed all necessary information about S into s to fit $p_S(x)$. To input information S to μ , we sample a point cloud containing m points on S — this enables us to train both μ and v with only point clouds. Specifically, given a dataset containing N point clouds, $\mathcal{X}^1, \dots, \mathcal{X}^N$, where \mathcal{X}^i contains ni.i.d. samples $x_1^i, \dots x_n^i \sim p_{S^i}(x)$ of shape S^i , we maximize the variational lower bound of the log-likelihood of the empirical distribution:

$$\max_{\theta} \mathbb{E} \underset{x \sim p_{\mathcal{S}}(x)}{\mathbb{E}} \log p_{\theta}(x|\mathcal{S}) \tag{4}$$

$$\approx \mathbb{E} \underset{S}{\mathbb{E}} \underset{x \sim p_{S}(x)}{\mathbb{E}} \log \int_{s} p_{\theta}(x, s | \mathcal{Z}) ds$$
 (5)

$$= \mathbb{E} \underset{x \sim p_{\mathcal{S}}(x)}{\mathbb{E}} \log \int_{s} p_{\theta}(x|s) p_{\theta}(s|\mathcal{Z}) ds$$
 (6)

$$= \mathbb{E} \underset{\mathcal{S}}{\mathbb{E}} \sup_{x \sim p_{\mathcal{S}}(x)} \log \int_{s} p_{\theta}(x|s) p_{\theta}(s|\mathcal{Z}) \frac{q_{\theta}(s|\mathcal{Y})}{q_{\theta}(s|\mathcal{Y})} ds \tag{7}$$

$$\geq \mathbb{E} \underset{x \sim p_{\mathcal{S}}(x)}{\mathbb{E}} \underset{s \sim q(s|\mathcal{Y})}{\mathbb{E}} \log p_{\theta}(x|s) - KL(q_{\theta}(s|\mathcal{Y})||p_{\theta}(s|\mathcal{Z})),$$

(8)

where \mathcal{Y} and \mathcal{Z} are independently sampled point clouds from $p_{\mathcal{S}}(x)$. The approximation in Equation (5) is from using \mathcal{Z} as \mathcal{S} and is controlled by the density of \mathcal{Z} . We apply Jensen's inequality at Equation (8). Since all models are jointly trained, we use θ to represent all learnable parameters. We use flow matching (3) to learn $p_{\theta}(x|s)$, we parameterize $q_{\theta}(s|\mathcal{Y})$ as a Gaussian distribution $\mathcal{N}(s; \mu_{\theta}(\mathcal{Y}), \sigma^2 I)$ and $p_{\theta}(s|\mathcal{Z})$ as $\mathcal{N}(s; \mu_{\theta}(\mathcal{Z}), \sigma^2 I)$. Under this parameterization, the KL divergence in Equation (8) is reduced to $\frac{1}{\sigma^2} \|\mu_{\theta}(\mathcal{Y}) - \mu_{\theta}(\mathcal{Z})\|^2$. This is intuitive as two point clouds sampled from the same shape should produce similar Shape Tokens. To regularize the shape-token space, we also add a KL-divergence $KL(q_{\theta}(s|\mathcal{Y}) \mid\mid p(s))$, where p(s) is the prior distribution of s, an isometric Gaussian distribution. We utilize a weighted sum of the KL divergence terms $(10^{-3} \text{ for Equation (8) and } 10^{-4} \text{ for the prior term) in the}$ training objective and set $\sigma = 10^{-3}$ empirically.

Architecture. The architecture of the shape tokenizer $\mu(\cdot) \to s$ and the flow-matching velocity estimator f are illustrated in Figure 2. The shape tokenizer has a similar architecture as a PerceiverIO architecture [34]. We learn an array of initial queries that retrieve information from the input point cloud representing the shape with a cross attention block. Two self-attention blocks are added after each cross attention block. A linear layer projects the output of the last self attention block to ST.

The velocity estimator v takes the ST s and a 3D location x as input and outputs the estimated 3D velocity at x. We use x as query of a cross attention block (and s as key and value). Note that there is no self attention in the velocity decoder to keep the velocity estimation at each 3D location independent to each other, making p(x|s) a 3D distribution (instead of a joint distribution of n locations). The flow matching time t is supplied to the velocity estimator through adaptive layer normalization.

4.1. Evaluation of shape tokenizers

We first train a shape tokenizer on the ShapeNet dataset [12], which contains 55 classes of objects. For fair comparison, we use the same training data as LION [77], including point cloud normalization and train-evaluation splits. The training set contains 35,708 point clouds, and the test set contains 10,261 point clouds. All point clouds contain 15,000 points. We randomly sample 4,096 points without replacement from the 15,000 points, and we use

²In practice, we normalize S so it lies in $[-1, 1]^3$.

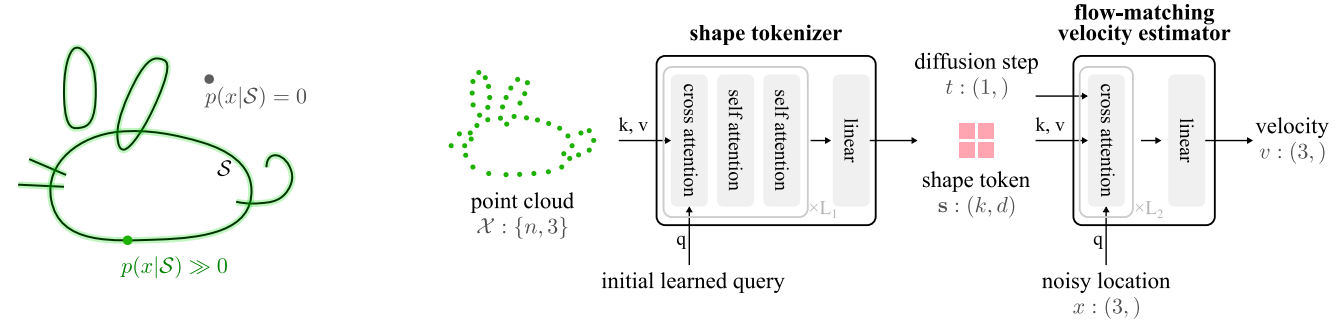


Figure 2. Overview of our architecture. (Left) We model a 3D shape as a probability density function that is concentrated on the surface, forming a delta function in 3D. (Right) Our tokenizer uses cross attention to aggregate information about the point cloud sampled on the shape into ST. The velocity estimator only use cross attention and MLP to maintain independence between points.

Table 1. Reconstruction error on ShapeNet.

	PointFlow [85]	ST	ST	ST	LION [77]	3DS2VSet [86]
latent dimension CD ($\times 10^{-3}$) \downarrow	512 1.75 ± 1.53	512 0.82 ± 1.19	$ \begin{array}{c c} 2048 \\ 0.75 \pm 0.53 \end{array} $	8192 0.65 ± 1.3	$\begin{array}{c} 8320 \\ 0.84 \pm 2.4 \end{array}$	32768 9.5

Table 2. Reconstruction error on Objaverse and GSO datasets. Chamfer distances are of unit 10^{-4} and the reference point clouds are boxnormalized to [-1, 1].

	Objaverse [20]			Google scanned objects [23]			
	CD@2048↓	CD@8192↓	normal (°)↓	CD@2048↓	CD@8192↓	Normal (°)↓	
Real 2048	5.1 ± 3.9	3.2 ± 2.5	25.3 ± 11.1	6.3 ± 2.9	4.0 ± 1.8	17.6 ± 8.74	
Real 8192	-	1.3 ± 1.1	20.5 ± 9.95	-	1.6 ± 0.77	14.3 ± 7.68	
ST (d = 8)	5.6 ± 4.0	1.8 ± 1.2	22.5 ± 10.2	6.7 ± 3.0	2.0 ± 0.85	15.1 ± 8.26	
ST (d = 16)	5.4 ± 4.0	1.6 ± 1.1	19.0 ± 8.84	6.6 ± 2.9	1.9 ± 0.83	13.9 ± 6.84	

the first 2048 points as input to the tokenizer and the rest as the reference when computing symmetric Chamfer Distance (CD). We train tokenizers with various total latent dimensions (number of ST multiplied by their dimension). We use 500 uniform steps of Heun's $2^{\rm nd}$ order method [36] to sample p(x|s).

We compare with Pointflow [85], as it is the closest to our method, and LION [77], which models the joint distribution of 2048 points. Both take 2048 input points and are trained on the same training data (normalization and split). PointFlow represents a shape as a latent vector of 512 dimensions, and LION represents a shape as a 128dimensional global latent and a local latent of 8192 total dimensions. We use the mean of the posterior distribution $(p(s|\mathcal{Z}))$ for all methods. As shown in Table 1, shape tokenization achieves similar chamfer distances while being 16× more compact than LION. The chamfer distances improve as we increase the total dimension of ST. We also report the chamfer distance from 3DShape2VecSet [86]. Note that our method is not directly comparable with theirs, which predicts occupancy (i.e., inside / outside of a watertight shape) and uses marching cube to find surfaces. This operation contributes to their larger chamfer distance.

We then train shape tokenizers on the Objaverse dataset [20], which contains 800k meshes with a wide variety of 3D shapes. Unlike existing methods that need watertight meshes for training (e.g., to compute signed dis-

tance functions or occupancy [79, 88, 89]), our method only requires point clouds. This significantly simplifies the training of shape tokenization — we are able to utilize all meshes in the training split of Objaverse and do not perform any pre-processing (e.g., smoothing the meshes, making the meshes watertight, etc.) besides box-normalization to [-1, 1]. We i.i.d. sample 200k points uniformly on the surface of the meshes to create a dataset of point clouds. We randomly select 640k meshes for training. We train two variants of shape tokenizers, both take 16,384 points as input and outputs 1024 tokens. The smaller tokenizer outputs 8-dimensional tokens and the other outputs 16-dimensional.

We evaluate the shape tokenizers on 600 held-out meshes in Objaverse and the entire Google Scanned Objects (GSO) dataset [23], which contains 1032 meshes. We sample without replacement 16384 + n points from each point cloud, the 16384 points are used as input to the tokenizer and the n points are used as reference when computing chamfer distance. Since there are no publicly available baselines trained on Objaverse, we obtain a baseline by comparing with real point clouds that are sampled from the surfaces of certain sizes (shown as Real in Table 2). When the number of points is the same as the reference point cloud, it provides an upperbound of the performance, and when the number points is smaller than the reference point clouds, we randomly sample with replacement to match the number of points in the reference number. This provides a strong baseline as all points are real and lie on the surface. As can be seen in Table 2 and Figure 3, shape tokenization reconstructs the 3D shapes well, we observe close chamfer distances to the upper bounds, and increasing dimension of ST improves chamfer distances.

4.2. Analysis

We analyze properties of shape tokenization—modeling 3D shapes as probability density functions with flow matching.

Surface normal. First we show that the connection between the flow matching velocity and the surface normal.

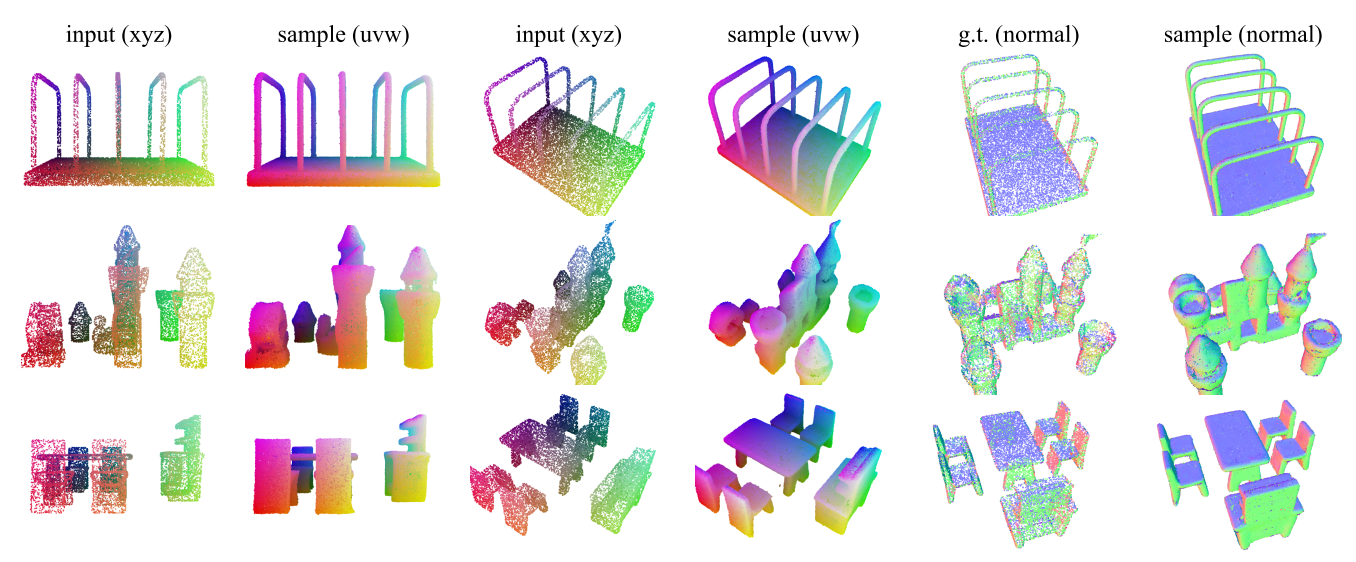


Figure 3. Reconstruction, densification, and normal estimation of unseen point clouds in GSO dataset. For each row, we are given a point cloud containing 16,384 points (xyz only), we compute ST and i.i.d. sample the resulted p(x|s) for 262,144 points. Different columns render the input and the sampled point clouds from different view points. Indicated by the label in the parenthesis, we color the input points according to their xyz coordinates and the sampled points according to their initial noise's uvw coordinates and their estimated normal (last two columns). Note that we do not provide normal as input to the shape tokenizer. Mesh credits [23].

Specifically, since $p(x|\mathcal{S})$ is a 3D delta function, the direction of the score function $\nabla_x \log p(x|\mathcal{S})$ aligns with the surface normal. We use the formula derived by Ma et al. [52] to convert velocity to score function and result in

$$\hat{n}(x) = \frac{\boldsymbol{\nabla}_x \log p_1(x|s)}{\|\boldsymbol{\nabla}_x \log p_1(x|s)\|} = \text{normalize}(\alpha_1 v(x;t \to 1) - \dot{\alpha}_1 x). \tag{9}$$

The expression motivates us to choose the generalized variance preserving path $(\alpha_t = \sin(\frac{\pi}{2}t))$ and $\sigma_t = \cos(\frac{\pi}{2}t))$ [2, 52] such that $\dot{\alpha}_1 = 0$ and the decoder directly estimates the normal direction when t = 1.

We utilize the property to estimate surface normal at the sampled points. Table 2 shows the angle between the estimated normal at sampled points and the ground truth normal, which is that of the closest point in the real point cloud. Notice the sampled points may not lie exactly on surfaces. Our baseline is to compute vertex normal from real point cloud by fitting a plane locally using Open3D [91]. It is a standard method when getting point clouds without vertex normal and is a strong baseline. As can be seen from the table, modeling entire 3D shape enables ST to outperform the strong real baseline when the number of points is small.

Log-likelihood. Our formulation using flow-matching enables using the instantaneous change of variable [15] to calculate the exact log-likelihood $\log p(x|s)$ at any 3D location, enabling us to estimate the probability of $x \in \mathcal{S}$ by integrating an ODE. Since our distribution is 3-dimensional, we can calculate the exact divergence with automatic differentiation with little cost instead of using a trace estimator as

by Song et al. [72]. The capability to evaluate log-likelihood at any location is useful for removing noisy points, e.g., due to the finite number of steps used for the ODE integration. We also notice that in practice we can get good estimation of the log-likelihood by integrating the ODE for log-likelihood estimation with much fewer steps (e.g., 25). In the paper, we use the technique to filter point clouds sampled from p(x|s) to filter the stray/noisy points caused by numerically integrating the ODE when sampling p(x|s). Please see prefiltered point clouds in the supplemental material.

UVW mapping. Since our velocity estimator is a neural network and thus is uniformly Lipschitz continuous in x and continuous in t, the ODE has non-intersecting integration trajectories and bijective mapping between the initial noise space and the 3D shape space [15]. This means that given any 3D location in the 3D space (i.e., xyz), we can traverse the ODE trajectory (2) back to a unique location in initial noise 3D space (that we call uvw to differentiate from xyz). Additionally, since the trajectories do not intersect, the mapping varies smoothly. Inspired by the property, we choose to use a uniform distribution within [-1, 1] as our initial noise distribution $e(\epsilon)$. This allows us to map each xyz to a location in a uvw-cube. One example is shown in Figure 4. We also use the property to color the sampled point clouds by their initial uvw locations (rgb = (uvw + 1) / 2). As can be seen in the figures, the uvw mapping varies smoothly across xyz. We think the uvw-mapping is an interesting property and worth noting in the paper, as it is automatically discovered by shape tokenization and resembles the UV-mapping technique used for texture interpolation.

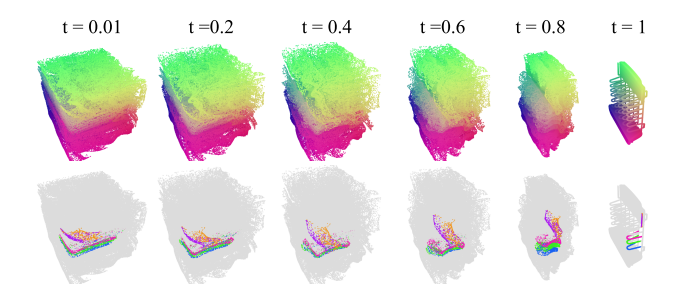


Figure 4. The ODE integration trajectory defines a mapping from xyz (data) to uvw (noise). Mesh credits [23].

5. Experiments

We apply ST to represent 3D in three applications, 3D shape generation (single-image-to-3D or unconditional generation) (Section 5.1), 3D CLIP (Section 5.2), and neural rendering (Section 5.3). Our goal is to demonstrate a variety of capabilities enabled by ST and further motivate future work. In all tasks, ST achieves competitive performance compared to models specifically designed for each task.

5.1. Token Generation with Latent Flow-Matching

To demonstrate our ST is compatible with generative models, we train Latent Flow-Matching (LFM) models that generate ST. We train an unconditional LFM on ShapeNet dataset (55 classes) [12] and an image-conditioned LFM on Objaverse dataset [20]. We use the same training splits as those used when training the corresponding shape tokenizers in Section 4. We build our velocity estimator based on the Diffusion Transformer architecture (DiT) [60] with AdaLN-single [14] and SwiGLU [69]. For the imageconditioned model, we use DINOv2 [59] to extract image features of each non-overlapping patch, and we encode the patch center rays' origins and directions with Fourier positional embedding and Plucker ray embedding [62], respectively. We also learn a linear layer to extract additional information from the image patches. The DINO feature, the output of the linear layer, and the ray embedding of each patch are concatenated along feature dimension to form a vector c. In each block, a cross-attention layer attends to cof all patches to gather image information. For each mesh in Objaverse, we render four images, each with 40 degrees field of view, 448×448 resolution, at 3.5 units on the opposite sides of x and z axes looking at the origin. We train the models with AdamW optimizer [48] with learning rate 10^{-4} with weight decay 0.01. The model is trained with batch size 128 for 200k iterations on ShapeNet and batch size 1024 for 1.2M iterations on Objaverse. During sampling, we apply Heun's 2nd order method [36] to sample both tokens (250 steps) and point clouds (100 steps).

Table 3 shows the unconditional generation results on ShapeNet. We compare with LION [77] and DPF [92].

Table 3. Unconditional generation on ShapeNet. For MMD-CD, the unit is 10^{-3} , and that for MMD-EMD is 10^{-2} .

	MMD ↓		COV ↑ (%)		1-NNA ↓ (%)	
Model	CD	EMD	CD	EMD	CD	EMD
LION [77]	3.4336	2.0953	48.0	52.2	58.25	57.75
DPF [92]	3.2586	2.1328	49.0	50.4	54.65	55.70
ST (ours)	3.2102	2.0847	50.8	54.6	57.80	55.55

Table 4. Single-image-conditioned generation on Objaverse.

Model	ULIP-I↑	P-FID↓	P-IS↑
Shap-E [35]	0.1307	-	-
Michelangelo [89]	0.1899	-	-
CLAY [88]	0.2066	0.9946	-
ST (ours)	0.3214	0.7664	11.4415

Specifically, LION is a latent diffusion model that models the joint distribution of a fixed size point set, and DPF is our implementation of [92] that directly models the coordinates of 3D points. Our model takes 32 ST of dimension 64; it has ~110M parameters, which is similar to the sizes of LION and DPF. We measure Minimum Matching Distance (MMD), Coverage (COV), and 1-Nearest Neighbor Accuracy (1-NNA) [85], using the same reference set as used by Vahdat et al. [77]. For each method, we sample point clouds containing 2048 points for 1000 samples in test set. As can be seen, our model achieves better performance than LION despite having a more compact latent space. Our model also achieves competitive performance with the ambient-space model, DPF, that is designed to learn the point distribution without a separately learned encoder.

Table 4 shows the quantitative results of single-image-conditioned generation on Objaverse. Due to the wide diversity of objects in Objaverse, we measure the quality of generated point clouds with ULIP-I [84], P-FID [58], and P-IS [58]. We use the PointNet++ provided by Nichol et al. [58] to measure P-FID and P-IS, which measures qualities of point clouds. We use ULIP-2 [84] to extract point-cloud embedding and measure cosine similarity with the conditioned image's CLIP embedding. This evaluates the similarity between the generated point cloud and the input image. Our LFM model generates ST of dimension 1024×16 . As can be seen from the table, our model performs strongly compared to existing baselines.

Figure 5 shows examples of our single-image to point cloud results. Our model generates point clouds that highly resemble the conditioning images and have plausible 3D shapes. Moreover, as shown in Figure 14, our model generates diverse samples when the conditioning is ambiguous (*e.g.*, surfaces invisible in the conditioning images). For example, the model generates rooms furnished differently and Buddha with different gestures. See the supplemental material for videos of more generated point clouds.

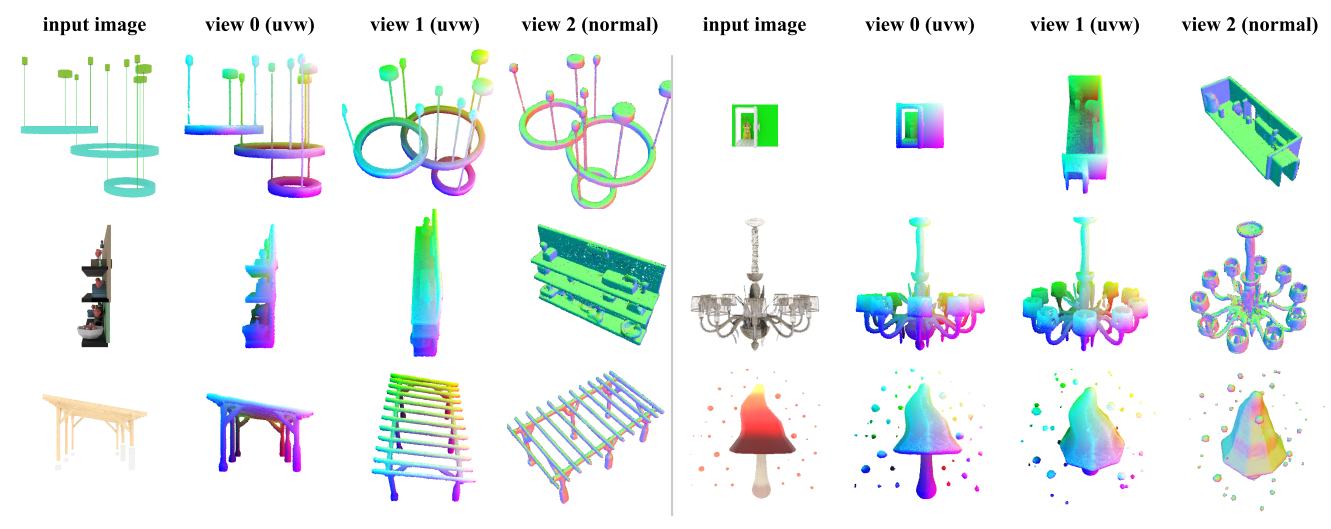


Figure 5. Single-image to 3D point cloud results on unseen meshes in Objaverse. We color the points with RGB color that indicates the original location of the point in the initial noise space. Mesh credits [4, 8, 25, 26, 29, 71].

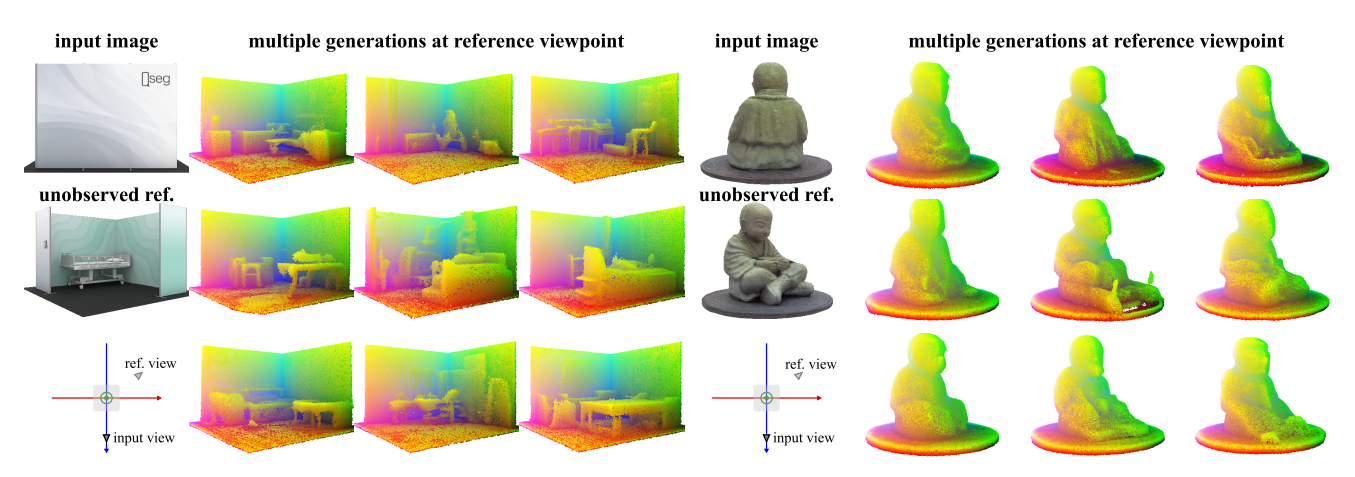


Figure 6. We generated 9 point clouds independently from the same input image (top left image of each set). We provide the rendered image of the meshes at the same viewpoint as a reference (middle left). No human selection was conducted, all 9 generated point clouds are shown. Note that the model does not observe the reference images. Mesh credits [22, 24].

5.2. 3D CLIP

3D-CLIP aims to align shape embeddings with image and text embeddings of a pretrained CLIP model [33]. The shape encoder takes a point cloud as input and outputs an embedding. We replace the shape encoder of an existing 3D-CLIP pipeline, OpenShape [44], with our shape tokenizer (1024×16) and an MLP.³ The MLP takes the concatenated ST as an input vector and has 4 layers of feature dimension 4096, and finally a linear layer output the embedding of dimension 1280. Note that we only train the MLP, and thus we are able to use a large batch size (600 per GPU). We use the same training recipe and datasets

as OpenShape. We train two models, one on Objaverse and ShapeNet datasets, and the other additionally on 3D-FUTURE [27] and ABO [19]. We use the same text captions as OpenShape. The models are trained for 2 weeks using 8 A100 GPUs.

Table 5 shows the zero-shot text classification results using the learned shape embedding. As can be seen, the model trained with ST as the 3D representation achieves comparable performance as OpenShape that uses a specifically trained PointBert encoder. We notice that our accuracy on ModelNet-40 reached 83.3% after training for 2 days and started decreasing afterwards, while the accuracy on Objaverse-LVIS kept increasing during the entire training. Since ModelNet40 is not part of the training set, this indicates a distribution mismatch between Objaverse-LVIS and ModelNet40, we believe an in-depth analysis of this

³Though ULIP-2 [84] has demonstrated better performance and has an improved text corpus, part of its training pipeline is not available. Since our goal is to demonstrate feasibility, we choose OpenShape [44] for its better maintained codebase.

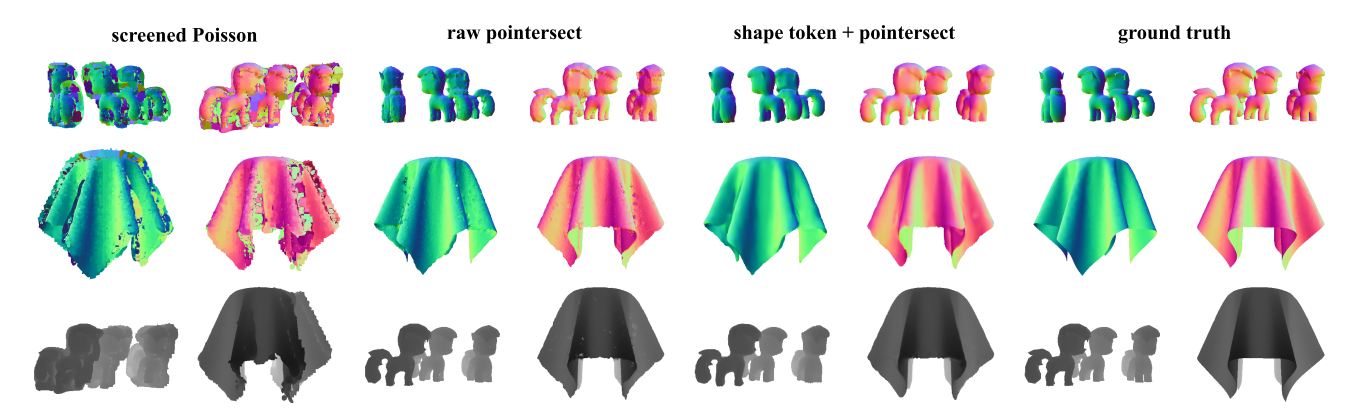


Figure 7. Given a point cloud containing 16,384 points (xyz only), camera pose and intrinsics, we process rays corresponding to each pixel individually and rasterize depth (bottom row) and normal (top two rows) map images. Mesh credits [10, 68].

Table 5. Zero-shot text classification. The first row block shows comparison between OpenShape with a jointly trained PointBERT encoder and OpenShape with ST + MLP encoder. The second row block include other current methods for reference.

			Objaverse-LVIS		ModelNet40	
Method	Input	Training Data	top-1	top-5	top-1	top-5
OpenShape + PointBERT [44]	xyz	[20], [11], [27], [19], [44]	42.6	73.1	84.7	97.4
OpenShape + ST	xyz	[20], [11], [44]	47.9	75.1	80.6	94.6
OpenShape + ST	xyz	[20], [11], [27], [19], [44]	48.4	75.5	78.6	93.4
ULIP + PointBERT [83]	xyz	[20], [11], [84]	34.9	61.0	69.6	85.9
OpenShape + PointBERT [44]	xyzrgb	[20], [11] [44]	46.5	76.3	82.6	96.9
OpenShape + PointBERT [44]	xyzrgb	[20], [11], [27], [19], [44]	46.8	77.0	84.4	98.0
ULIP-2 + PointBERT [84]	xyz	[20], [11], [84]	48.9	77.1	84.1	97.3

observation is out of the scope of the paper.

5.3. Neural rendering

Ray-shape intersection is an important operator in graphics. We demonstrate the capability of estimating the intersection point between a ray and the underlying 3D geometry represented by ST. We take an existing method, Pointersect [13], that uses the input point cloud and a ray as input to a transformer to estimate intersection points, and use ST to represent the input point cloud. Specifically, we train a transformer consisting of 4 blocks of cross-attention layers, each is paired with a 2-layer MLP. The cross attention takes the Plucker embedding of a single ray as query and attends to the ST. In other words, individual rays are independently processed. A final linear layer outputs estimations of whether the ray hits any surface, the ray-traveling distance to the first intersection point, and the surface normal. Given a camera pose and intrinsics, we process rays corresponding to each pixel individually and rasterize depth and normal map images. The results are shown in Table 6 and Figure 7. With ST as its 3D representation, the model is able to estimate a smoother normal map, robust to local variations of point clouds.

Table 6. Ray-shape intersection on unseen Objaverse shapes.

	Poisson [37]	Pointersect [13]	ST (ours) + Pointersect [13]
Depth (RMSE) ↓	0.16 ± 0.15	0.064 ± 0.066	0.053 ± 0.055
Normal (angle (°))↓	26.0 ± 14.1	17.7 ± 12.3	15.7 ± 12.3
Hit (acc (%)) ↑	91.1 ± 10.6	99.4 ± 1.20	99.3 ± 1.19

6. Discussion

Shape tokenization is a novel data-driven method for 3D shape representation. It lies on the opposite end of the spectrum from most existing 3D representations, which explicitly model geometry (*e.g.*, meshes, SDFs) or rendering formulations (*e.g.*, 3D Gaussians, NeRF). Despite being motivated by machine learning, we show that Shape Tokens possess properties that are tightly connected to 3D geometry, such as surface normals and UVW mapping. Shape tokenization and the connection between flow matching and 3D geometry provide an interesting and new viewpoint of 3D representations. Across a number of downstream tasks, Shape Tokens demonstrates competitive performance with task-specific representations.

Limitations. Current Shape Tokens consider geometry only; extending to color is for future work. We need to integrate ODEs when sampling point clouds, shape tokens, or computing log-likelihood, this means it takes longer times to generate a point cloud than feed-forward methods. Utilizing methods like distillation or advancement in diffusion models to improve sampling efficiency is also future work.

References

- Home Design 3D. New project (10), n.d. Licensed under CC Attribution-NonCommercial-ShareAlike 4.0 International (CC BY-NC-SA 4.0), 20
- [2] Michael Albergo and Eric Vanden-Eijnden. Building normalizing flows with stochastic interpolants. In *International Conference on Learning Representations (ICLR)*, 2023. 5
- [3] andresblancof. Gohome1, n.d. Licensed under Creative Commons Attribution 4.0 International (CC BY 4.0). 1
- [4] anyaachan. Red low-poly glowing mushroom, n.d. Licensed under Creative Commons Attribution 4.0 International (CC BY 4.0). 7
- [5] WHA Arquitectos. 20_librero repisas, n.d. Licensed under Creative Commons Attribution 4.0 International (CC BY 4.0). 1
- [6] bennett_graham. Bennett graham bracelet 2, n.d. Licensed under Creative Commons Attribution 4.0 International (CC BY 4.0).
- [7] Binkley-Spacetrucker. Galactic truckstop restrooms, n.d.. Licensed under Creative Commons Attribution 4.0 International (CC BY 4.0). 20
- [8] Binkley-Spacetrucker. Galactic truckstop restrooms, n.d.. Licensed under Creative Commons Attribution 4.0 International (CC BY 4.0).
- [9] Robert Bridson, Sebastian Marino, and Ronald Fedkiw. Simulation of clothing with folds and wrinkles. In ACM SIG-GRAPH 2005 Courses, pages 3–es. 2005. 1
- [10] Caitlin. test fabric 1, n.d. Licensed under Creative Commons Attribution 4.0 International (CC BY 4.0). 8
- [11] A. Chang, T. Funkhouser, L. Guibas, et al. Shapenet: An information-rich 3d model repository. arXiv, 2015. 8
- [12] Angel X. Chang, Thomas Funkhouser, Leonidas Guibas, Pat Hanrahan, Qixing Huang, Zimo Li, Silvio Savarese, Manolis Savva, Shuran Song, Hao Su, Jianxiong Xiao, Li Yi, and Fisher Yu. ShapeNet: An Information-Rich 3D Model Repository. Technical Report arXiv:1512.03012 [cs.GR], Stanford University — Princeton University — Toyota Technological Institute at Chicago, 2015. 2, 3, 6
- [13] Jen-Hao Rick Chang, Wei-Yu Chen, Anurag Ranjan, Kwang Moo Yi, and Oncel Tuzel. Pointersect: Neural rendering with cloud-ray intersection. In *IEEE Conference on Computer Vision and Pattern Recognition (CVPR)*, pages 8359–8369, 2023. 8, 13
- [14] Junsong Chen, Jincheng Yu, Chongjian Ge, Lewei Yao, Enze Xie, Yue Wu, Zhongdao Wang, James Kwok, Ping Luo, Huchuan Lu, et al. Pixart-alpha: Fast training of diffusion transformer for photorealistic text-to-image synthesis. arXiv preprint arXiv:2310.00426, 2023. 6
- [15] Ricky TQ Chen, Yulia Rubanova, Jesse Bettencourt, and David K Duvenaud. Neural ordinary differential equations. Advances in Neural Information Processing Systems (NeurIPS), 31, 2018. 5
- [16] Ricky T. Q. Chen, Yulia Rubanova, Jesse Bettencourt, and David Duvenaud. Neural ordinary differential equations. In Advances in Neural Information Processing Systems (NeurIPS), 2018. 13

- [17] Sijin Chen, Xin Chen, Anqi Pang, Xianfang Zeng, Wei Cheng, Yijun Fu, Fukun Yin, Yanru Wang, Zhibin Wang, Chi Zhang, et al. Meshxl: Neural coordinate field for generative 3d foundation models. arXiv preprint arXiv:2405.20853, 2024. 2
- [18] Julian Chibane, Gerard Pons-Moll, et al. Neural unsigned distance fields for implicit function learning. Advances in Neural Information Processing Systems (NeurIPS), 33: 21638–21652, 2020. 1
- [19] Jasmine Collins, Shubham Goel, Kenan Deng, Achleshwar Luthra, Leon Xu, Erhan Gundogdu, Xi Zhang, Tomas F Yago Vicente, Thomas Dideriksen, Himanshu Arora, et al. Abo: Dataset and benchmarks for real-world 3d object understanding. In *IEEE Conference on Computer Vision and Pattern Recognition (CVPR)*, pages 21126–21136, 2022. 7,
- [20] Matt Deitke, Dustin Schwenk, Jordi Salvador, Luca Weihs, Oscar Michel, Eli VanderBilt, Ludwig Schmidt, Kiana Ehsani, Aniruddha Kembhavi, and Ali Farhadi. Objaverse: A universe of annotated 3d objects. arXiv preprint arXiv:2212.08051, 2022. 2, 4, 6, 8
- [21] Jiajun Deng, Shaoshuai Shi, Peiwei Li, Wengang Zhou, Yanyong Zhang, and Houqiang Li. Voxel r-cnn: Towards high performance voxel-based 3d object detection. In *Proceedings of the AAAI conference on artificial intelligence*, pages 1201–1209, 2021. 1
- [22] Onironauta digital. Monk statue, n.d. Licensed under Creative Commons Attribution 4.0 International (CC BY 4.0).
- [23] Laura Downs, Anthony Francis, Nate Koenig, Brandon Kinman, Ryan Hickman, Krista Reymann, Thomas B McHugh, and Vincent Vanhoucke. Google scanned objects: A high-quality dataset of 3d scanned household items. In *International Conference on Robotics and Automation (ICRA)*, pages 2553–2560. IEEE, 2022. 4, 5, 6
- [24] exhibitbook. Qseg isolation single full print, n.d. Licensed under Creative Commons Attribution 4.0 International (CC BY 4.0). 7
- [25] fedomo.ru. Lyustra 2054-10p favourite, n.d.. Licensed under Creative Commons Attribution 4.0 International (CC BY 4.0). 7
- [26] fedomo.ru. Svetilnik 3885/25la odeon light, n.d.. Licensed under Creative Commons Attribution 4.0 International (CC BY 4.0). 7
- [27] Huan Fu, Rongfei Jia, Lin Gao, Mingming Gong, Binqiang Zhao, Steve Maybank, and Dacheng Tao. 3d-future: 3d furniture shape with texture. *International Journal of Computer Vision (IJCV)*, 129:3313–3337, 2021. 7, 8
- [28] Ruiqi Gao*, Aleksander Holynski*, Philipp Henzler, Arthur Brussee, Ricardo Martin-Brualla, Pratul P. Srinivasan, Jonathan T. Barron, and Ben Poole*. Cat3d: Create anything in 3d with multi-view diffusion models. Advances in Neural Information Processing Systems (NeurIPS), 2024. 2
- [29] MARTINICE GROUP. Op220667, n.d. Licensed under Creative Commons Attribution 4.0 International (CC BY 4.0).

- [30] Eran Guendelman, Robert Bridson, and Ronald Fedkiw. Nonconvex rigid bodies with stacking. ACM Transactions on Graphics (TOG), 22(3):871–878, 2003.
- [31] Yicong Hong, Kai Zhang, Jiuxiang Gu, Sai Bi, Yang Zhou, Difan Liu, Feng Liu, Kalyan Sunkavalli, Trung Bui, and Hao Tan. LRM: Large reconstruction model for single image to 3d. In *International Conference on Learning Representa*tions (ICLR), 2024. 2
- [32] Ka-Hei Hui, Aditya Sanghi, Arianna Rampini, Ka-mal Rahimi Malekshan, Zhengzhe Liu, Hooman Shayani, and Chi-Wing Fu. Make-a-shape: a ten-million-scale 3d shape model. In *International Conference on Machine Learning (ICML)*, 2024. 12, 13
- [33] Gabriel Ilharco, Mitchell Wortsman, Ross Wightman, Cade Gordon, Nicholas Carlini, Rohan Taori, Achal Dave, Vaishaal Shankar, Hongseok Namkoong, John Miller, Hannaneh Hajishirzi, Ali Farhadi, and Ludwig Schmidt. Openclip, 2021. If you use this software, please cite it as below.
- [34] A. Jaegle, S. Borgeaud, J. Alayrac, et al. Perceiver io: A general architecture for structured inputs & outputs. In *International Conference on Learning Representations (ICLR)*, 2022. 3
- [35] Heewoo Jun and Alex Nichol. Shap-e: Generating conditional 3d implicit functions. *arXiv preprint arXiv:2305.02463*, 2023. 6
- [36] Tero Karras, Miika Aittala, Timo Aila, and Samuli Laine. Elucidating the design space of diffusion-based generative models. Advances in Neural Information Processing Systems (NeurIPS), 35:26565–26577, 2022. 4, 6
- [37] Michael Kazhdan and Hugues Hoppe. Screened poisson surface reconstruction. ACM Transactions on Graphics (TOG), 32(3):1–13, 2013. 8, 13
- [38] Bernhard Kerbl, Georgios Kopanas, Thomas Leimkühler, and George Drettakis. 3d gaussian splatting for real-time radiance field rendering. ACM Transactions on Graphics, 42 (4), 2023. 1
- [39] Byung-soo Kim, Pushmeet Kohli, and Silvio Savarese. 3d scene understanding by voxel-crf. In *IEEE International Conference on Computer Vision (ICCV)*, pages 1425–1432, 2013. 1
- [40] Christoph Lassner and Michael Zollhofer. Pulsar: Efficient sphere-based neural rendering. In *IEEE Conference on Com*puter Vision and Pattern Recognition (CVPR), pages 1440– 1449, 2021. 1
- [41] Chun-Liang Li, Manzil Zaheer, Yang Zhang, Barnabas Poczos, and Ruslan Salakhutdinov. Point cloud gan. arXiv preprint arXiv:1810.05795, 2018. 1
- [42] Jiahao Li, Hao Tan, Kai Zhang, Zexiang Xu, Fujun Luan, Yinghao Xu, Yicong Hong, Kalyan Sunkavalli, Greg Shakhnarovich, and Sai Bi. Instant3d: Fast text-to-3d with sparse-view generation and large reconstruction model. arXiv preprint arXiv:2311.06214, 2023. 2, 12
- [43] Yaron Lipman, Ricky T. Q. Chen, Heli Ben-Hamu, Maximilian Nickel, and Matt Le. Flow matching for generative modeling. In *International Conference on Learning Representations (ICLR)*, 2023. 3

- [44] Minghua Liu, Ruoxi Shi, Kaiming Kuang, Yinhao Zhu, Xuanlin Li, Shizhong Han, Hong Cai, Fatih Porikli, and Hao Su. Openshape: Scaling up 3d shape representation towards open-world understanding. *Advances in Neural Information Processing Systems (NeurIPS)*, 36, 2024. 2, 7, 8
- [45] Ruoshi Liu, Rundi Wu, Basile Van Hoorick, Pavel Tok-makov, Sergey Zakharov, and Carl Vondrick. Zero-1-to-3: Zero-shot one image to 3d object. In *IEEE International Conference on Computer Vision (ICCV)*, pages 9298–9309, 2023.
- [46] Yu-Tao Liu, Li Wang, Jie Yang, Weikai Chen, Xiaoxu Meng, Bo Yang, and Lin Gao. Neudf: Leaning neural unsigned distance fields with volume rendering. In *IEEE Conference* on Computer Vision and Pattern Recognition (CVPR), pages 237–247, 2023. 1
- [47] Zhijian Liu, Haotian Tang, Yujun Lin, and Song Han. Point-voxel cnn for efficient 3d deep learning. *Advances in Neural Information Processing Systems (NeurIPS)*, 32, 2019. 1
- [48] I Loshchilov. Decoupled weight decay regularization. *arXiv* preprint arXiv:1711.05101, 2017. 6
- [49] Ilya Loshchilov and Frank Hutter. Decoupled weight decay regularization. In *International Conference on Learning Representations (ICLR)*, 2019. 17
- [50] S. Luo and W. Hu. Diffusion probabilistic models for 3d point cloud generation. In *IEEE Conference on Computer Vision and Pattern Recognition (CVPR)*, 2021. 2
- [51] Shitong Luo and Wei Hu. Diffusion probabilistic models for 3d point cloud generation. In *IEEE Conference on Computer Vision and Pattern Recognition (CVPR)*, pages 2837–2845, 2021. 2
- [52] Nanye Ma, Mark Goldstein, Michael S Albergo, Nicholas M Boffi, Eric Vanden-Eijnden, and Saining Xie. SiT: Exploring flow and diffusion-based generative models with scalable interpolant transformers. European Conference on Computer Vision (ECCV), 2024. 3, 5
- [53] madexc. domik-house, n.d. Licensed under Creative Commons Attribution 4.0 International (CC BY 4.0).
- [54] Lars Mescheder, Michael Oechsle, Michael Niemeyer, Sebastian Nowozin, and Andreas Geiger. Occupancy networks: Learning 3d reconstruction in function space. In IEEE Conference on Computer Vision and Pattern Recognition (CVPR), pages 4460–4470, 2019. 1
- [55] Ben Mildenhall, Pratul P. Srinivasan, Matthew Tancik, Jonathan T. Barron, Ravi Ramamoorthi, and Ren Ng. Nerf: Representing scenes as neural radiance fields for view synthesis. In European Conference on Computer Vision (ECCV), 2020. 1
- [56] Paritosh Mittal, Yen-Chi Cheng, Maneesh Singh, and Shubham Tulsiani. AutoSDF: Shape priors for 3d completion, reconstruction and generation. In *IEEE Conference on Computer Vision and Pattern Recognition (CVPR)*, 2022. 1
- [57] Charlie Nash, Yaroslav Ganin, SM Ali Eslami, and Peter Battaglia. Polygen: An autoregressive generative model of 3d meshes. In *International Conference on Machine Learn*ing (ICML), pages 7220–7229. PMLR, 2020. 1
- [58] Alex Nichol, Heewoo Jun, Prafulla Dhariwal, Pamela Mishkin, and Mark Chen. Point-e: A system for generat-

- ing 3d point clouds from complex prompts. arXiv preprint arXiv:2212.08751, 2022. 2, 6, 12
- [59] Maxime Oquab, Timothée Darcet, Théo Moutakanni, Huy V. Vo, Marc Szafraniec, Vasil Khalidov, Pierre Fernandez, Daniel HAZIZA, Francisco Massa, Alaaeldin El-Nouby, Mido Assran, Nicolas Ballas, Wojciech Galuba, Russell Howes, Po-Yao Huang, Shang-Wen Li, Ishan Misra, Michael Rabbat, Vasu Sharma, Gabriel Synnaeve, Hu Xu, Herve Jegou, Julien Mairal, Patrick Labatut, Armand Joulin, and Piotr Bojanowski. DINOv2: Learning robust visual features without supervision. Transactions on Machine Learning Research, 2024. 6
- [60] William Peebles and Saining Xie. Scalable diffusion models with transformers. In *IEEE International Conference on Computer Vision (ICCV)*, pages 4195–4205, 2023. 6
- [61] Songyou Peng, Michael Niemeyer, Lars Mescheder, and Andreas Geiger Marc Pollefeys. Convolutional occupancy networks. In European Conference on Computer Vision (ECCV), 2020. 1
- [62] J. Plucker. Analytisch-Geometrische Entwicklungen, Erster Band. Creative Media Partners, LLC, 2018. 6, 17
- [63] Ben Poole, Ajay Jain, Jonathan T. Barron, and Ben Mildenhall. Dreamfusion: Text-to-3d using 2d diffusion. In International Conference on Learning Representations (ICLR), 2023.
- [64] Charles R Qi, Hao Su, Kaichun Mo, and Leonidas J Guibas. Pointnet: Deep learning on point sets for 3d classification and segmentation. In *IEEE Conference on Computer Vision* and Pattern Recognition (CVPR), 2017.
- [65] Xuanchi Ren, Jiahui Huang, Xiaohui Zeng, Ken Museth, Sanja Fidler, and Francis Williams. Xcube: Large-scale 3d generative modeling using sparse voxel hierarchies. In IEEE Conference on Computer Vision and Pattern Recognition (CVPR), 2024. 2
- [66] RodierGabrielle. Early morning by the lake, n.d. Licensed under Creative Commons Attribution 4.0 International (CC BY 4.0). 1
- [67] Robin Rombach, Andreas Blattmann, Dominik Lorenz, Patrick Esser, and Björn Ommer. High-resolution image synthesis with latent diffusion models. In *IEEE Conference* on Computer Vision and Pattern Recognition (CVPR), pages 10684–10695, 2022. 17
- [68] shakiller. Pony, n.d. Licensed under Creative Commons Attribution 4.0 International (CC BY 4.0). 8
- [69] Noam Shazeer. Glu variants improve transformer. arXiv preprint arXiv:2002.05202, 2020. 6
- [70] Yawar Siddiqui, Antonio Alliegro, Alexey Artemov, Tatiana Tommasi, Daniele Sirigatti, Vladislav Rosov, Angela Dai, and Matthias Nießner. Meshgpt: Generating triangle meshes with decoder-only transformers. In *IEEE Conference on Computer Vision and Pattern Recognition (CVPR)*, pages 19615–19625, 2024. 1, 2
- [71] SketchingSushi. Cali in the garden!, n.d. Licensed under Creative Commons Attribution 4.0 International (CC BY 4.0). 7
- [72] Yang Song, Jascha Sohl-Dickstein, Diederik P Kingma, Abhishek Kumar, Stefano Ermon, and Ben Poole. Score-based

- generative modeling through stochastic differential equations. In *International Conference on Learning Representations (ICLR)*, 2021. 5
- [73] Yongbin Sun, Yue Wang, Ziwei Liu, Joshua E Siegel, and Sanjay E Sarma. Pointgrow: Autoregressively learned point cloud generation with self-attention. In Winter Conference on Applications of Computer Vision, 2020.
- [74] Stanislaw Szymanowicz, Chrisitian Rupprecht, and Andrea Vedaldi. Splatter image: Ultra-fast single-view 3d reconstruction. In *IEEE Conference on Computer Vision and Pat*tern Recognition (CVPR), pages 10208–10217, 2024. 12
- [75] Jiaxiang Tang, Zhaoxi Chen, Xiaokang Chen, Tengfei Wang, Gang Zeng, and Ziwei Liu. Lgm: Large multi-view gaussian model for high-resolution 3d content creation. In *European Conference on Computer Vision (ECCV)*, pages 1–18. Springer, 2025. 2
- [76] A. Tewari, J. Thies, B. Mildenhall, P. Srinivasan, E. Tretschk, W. Yifan, C. Lassner, V. Sitzmann, R. Martin-Brualla, S. Lombardi, T. Simon, C. Theobalt, M. Nießner, J. T. Barron, G. Wetzstein, M. Zollhöfer, and V. Golyanik. Advances in neural rendering. *Computer Graphics Forum*, 41(2):703–735, 2022.
- [77] Arash Vahdat, Francis Williams, Zan Gojcic, Or Litany, Sanja Fidler, Karsten Kreis, et al. Lion: Latent point diffusion models for 3d shape generation. Advances in Neural Information Processing Systems (NeurIPS), 35:10021–10039, 2022. 2, 3, 4, 6
- [78] Ashish Vaswani, Noam Shazeer, Niki Parmar, Jakob Uszkoreit, Llion Jones, Aidan N Gomez, Łukasz Kaiser, and Illia Polosukhin. Attention is All You Need. Advances in Neural Information Processing Systems (NeurIPS), 30, 2017. 17
- [79] Shuang Wu, Youtian Lin, Feihu Zhang, Yifei Zeng, Jingxi Xu, Philip Torr, Xun Cao, and Yao Yao. Direct3d: Scalable image-to-3d generation via 3d latent diffusion transformer. arXiv preprint arXiv:2405.14832, 2024. 2, 4
- [80] Y. Xie, T. Takikawa, S. Saito, O. Litany, S. Yan, N. Khan, F. Tombari, J. Tompkin, V. Sitzmann, and S. Sridhar. Neural fields in visual computing and beyond. In *Computer Graphics Forum*, 2022. 1
- [81] Yinghao Xu, Zifan Shi, Wang Yifan, Sida Peng, Ceyuan Yang, Yujun Shen, and Wetzstein Gordon. Grm: Large gaussian reconstruction model for efficient 3d reconstruction and generation. arxiv: 2403.14621, 2024. 2, 12
- [82] Yinghao Xu, Hao Tan, Fujun Luan, Sai Bi, Peng Wang, Ji-ahao Li, Zifan Shi, Kalyan Sunkavalli, Gordon Wetzstein, Zexiang Xu, and Kai Zhang. DMV3d: Denoising multiview diffusion using 3d large reconstruction model. In *International Conference on Learning Representations (ICLR)*, 2024. 2
- [83] Le Xue, Mingfei Gao, Chen Xing, Roberto Martín-Martín, Jiajun Wu, Caiming Xiong, Ran Xu, Juan Carlos Niebles, and Silvio Savarese. Ulip: Learning a unified representation of language, images, and point clouds for 3d understanding. In *IEEE Conference on Computer Vision and Pattern Recog*nition (CVPR), pages 1179–1189, 2023. 8
- [84] Le Xue, Ning Yu, Shu Zhang, Artemis Panagopoulou, Junnan Li, Roberto Martín-Martín, Jiajun Wu, Caiming Xiong,

- Ran Xu, Juan Carlos Niebles, et al. Ulip-2: Towards scalable multimodal pre-training for 3d understanding. In *IEEE Conference on Computer Vision and Pattern Recognition (CVPR)*, pages 27091–27101, 2024. 6, 7, 8
- [85] Guandao Yang, Xun Huang, Zekun Hao, Ming-Yu Liu, Serge Belongie, and Bharath Hariharan. PointFlow: 3D point cloud generation with continuous normalizing flows. In *IEEE International Conference on Computer Vision (ICCV)*, 2019. 1, 2, 4, 6
- [86] Biao Zhang, Jiapeng Tang, Matthias Niessner, and Peter Wonka. 3dshape2vecset: A 3d shape representation for neural fields and generative diffusion models. ACM Transactions on Graphics (TOG), 42(4):1–16, 2023. 2, 4
- [87] Kai Zhang, Sai Bi, Hao Tan, Yuanbo Xiangli, Nanxuan Zhao, Kalyan Sunkavalli, and Zexiang Xu. Gs-lrm: Large reconstruction model for 3d gaussian splatting. In *European Conference on Computer Vision (ECCV)*, pages 1–19. Springer, 2025. 2
- [88] Longwen Zhang, Ziyu Wang, Qixuan Zhang, Qiwei Qiu, Anqi Pang, Haoran Jiang, Wei Yang, Lan Xu, and Jingyi Yu. CLAY: A controllable large-scale generative model for creating high-quality 3d assets. ACM Transactions on Graphics (TOG), 43(4):1–20, 2024. 2, 4, 6
- [89] Zibo Zhao, Wen Liu, Xin Chen, Xianfang Zeng, Rui Wang, Pei Cheng, BIN FU, Tao Chen, Gang YU, and Shenghua Gao. Michelangelo: Conditional 3d shape generation based on shape-image-text aligned latent representation. In Advances in Neural Information Processing Systems (NeurIPS), 2023. 2, 4, 6
- [90] Zibo Zhao, Wen Liu, Xin Chen, Xianfang Zeng, Rui Wang, Pei Cheng, Bin Fu, Tao Chen, Gang Yu, and Shenghua Gao. Michelangelo: Conditional 3d shape generation based on shape-image-text aligned latent representation. Advances in Neural Information Processing Systems (NeurIPS), 36, 2024.
- [91] Qian-Yi Zhou, Jaesik Park, and Vladlen Koltun. Open3D: A modern library for 3D data processing. arXiv:1801.09847, 2018. 5, 17
- [92] Peiye Zhuang, Samira Abnar, Jiatao Gu, Alex Schwing, Joshua M Susskind, and Miguel Angel Bautista. Diffusion probabilistic fields. In *International Conference on Learning Representations (ICLR)*, 2023. 6

A. Summary of appendix

In the supplemental material, we present details about:

- Videos of single-image-to-3D results on Objaverse test set (see index.html).
- Videos of single-image-to-3D results on Google Scanned Objects (see index.html). We also compare with recent single-image-to-3D methods, including Point-e [58], Splatter-image [74], and Make-a-Shape [32].
- Videos of reconstruction, densification, and uvw-xyz deformation of point clouds in Google Scanned Objects (see index.html).
- Videos of multiple independent samples from the same input image (see index.html).
- Videos of point clouds sampled from linear interpolated Shape Tokens. (see index.html).
- Videos of neural rendering results. (see index.html).
- Point cloud filtering results.
- Scaling experiments of single-image-to-3D.
- Architecture and training details of Shape Tokenizer.
- Runtime analysis.

B. Single-image-to-3D on Objaverse

In the attached offline website, we present ¿100 videos of single-image-to-3D results on the Objaverse test set. In the videos, we first show the input image, then the sampled point cloud from the sampled Shape Tokens from the input view. Finally, we rotate the viewpoints. As can be seen from the videos, our results follow input image closely from the input viewpoint and have plausible 3D structures when seen from other viewpoints. In the results, the Shape Tokens are sampled with 250 steps using Heun's method, and the point clouds are sampled with 100 steps using Heun's method. We use classifier free guidance with scale equal to 5.

C. Single-image-to-3D on GSO

In the attached offline website, Figure 8, Figure 9 and Figure 10, we present more than 20 single-image-to-3D results on Google Scanned Objects (GSO). We also present results from recent single-image-to-3D methods using the same input image:

- Point-e [58], which is trained on a proprietary dataset containing several millions meshes. It first generates 1024 points, then uses another model to upsample to 4096 points. It models the joint distribution of a point set with a fixed number of points and cannot sample arbitrary number of points.
- Splatter-image [74], which is a recent method that takes an image as input and predicts 3D Gaussian splats representing the scene. It also models RGB color. The model is trained on Objaverse. Along the same line of works as splatter images, recent methods [42, 81] often use an

additional multiview image diffusion model to generate multiview images from a single image, then apply the multiview images to a model that is similar to Splatterimage to construct 3D Gaussian splats. We think Splatterimage reasonably demonstrate the performance of such methodology without using the additional image diffusion model.

Make-a-Shape [32], which is a recent method that represents voxel grids of signed distance functions with packed and pruned wavelet coefficients. A diffusion model is learned to generate the representation given a single image. The model is trained on ¿10 million meshes from 18 datasets, including Objaverse.

We present these results for the reader's reference, and we want to emphasize that they are not intended for direct comparison. The models differ in their training data (e.g., Point-e is trained on a proprietary dataset) and underlying mechanisms (e.g., Splatter-image is not a generative model and our model assumes the input camera parameters are known). In general, we find it difficult to establish completely fair comparisons of image-to-3D methods. We hope our code and model release can help improve the situation. In the results, the Shape Tokens are sampled with 250 steps using Heun's method, and the point clouds are sampled with 100 steps using Heun's method. We use classifier free guidance with scale equal to 5.

D. Reconstruction and densification on GSO

In the attached offline website, we present ξ 20 videos of point clouds sampled from the Shape Tokens computed from input point clouds in Google Scanned Objects (GSO). The input point clouds contain 16,384 points, and we sample 262,144 points ($16\times$) to demonstrate the densification capability. We also color the point clouds with their initial coordinate in the noise space (uvw) to demonstrate the deformation trajectory from the noise space (uvw) to the ambient space (xyz). As can be seen, the trajectories smoothly vary in 3D.

E. Multiple samples from same image

In the attached offline website, we present results of point clouds sampled from independently sampled Shape Tokens from the same input image. The input images are from Objaverse test set. As can be seen, the model can generate diverse samples when the input image is ambiguous while matching the input image. In the results, the Shape Tokens are sampled with 250 steps using Heun's method, and the point clouds are sampled with 100 steps using Heun's method. We do not use classifier-free guidance in these examples.

F. Linear interpolation of Shape Tokens

Out of curiosity, we linear interpolate Shape Tokens computed by two distinct shapes. Specifically, given two Shape Tokens, s_1 and s_2 , we compute a series of Shape Tokens:

$$s(w) = (1 - w)s_1 + ws_2, (10)$$

where w varies from 0 to 1. We sample point clouds from the resulting Shape Tokens with the same initial noise (colored by their uvw coordinates) and render the video shown in the attached offline website.

G. Neural rendering results on Objaverse

In the attached offline website, we present results of neural rendered normal maps from input point clouds from Objaverse test set. We also present results from screened Poisson reconstruction [37] and Pointersect [13]. Screened Poisson reconstruction first reconstructs a mesh from the input point cloud, then renders the normal maps. Since the input point clouds do not contain vertex normal, we use Open3D to estimate vertex normal by computing principle components of local point clouds. Screened Poisson reconstruction is sensitive to the quality of the vertex normal. We use the implementation of screened Poisson reconstruction in Open3D with depth=7, and we remove the vertices with density in the last 5% percentile. We empirically find the settings produces slightly better results in our experiments.

Pointersect is a neural rendering method that takes a target ray and an input point and estimates the intersection point between the ray and the underlying shape represented by the point cloud. We find it preserve high frequency details in the rendered normal maps, but it is also sensitive to the input point cloud and thus its results often contain high frequency noise. Our neural rendering model takes a target ray and Shape Tokens computed from the input point cloud, and it estimates the intersection point between the ray and the underlying shape represented by the point cloud. The normal estimation is more robust to input-point configurations, however, we also observe smoothing in the rendered normal maps.

H. Point cloud filtering results

In Figure 11 and Figure 12, we show point clouds before and after filtering by the log-likelihood computed using the instantaneous change of variables technique [16]. In the results of the paper, we sample point clouds containing more than 200 thousands of points using numerical integration of the ordinary differential equations of flow matching with finite number of steps (e.g., 100). Since we sample individual points in the large number of points independently, a small number of points may contain error from the numerical integration. As a result, some points may be away

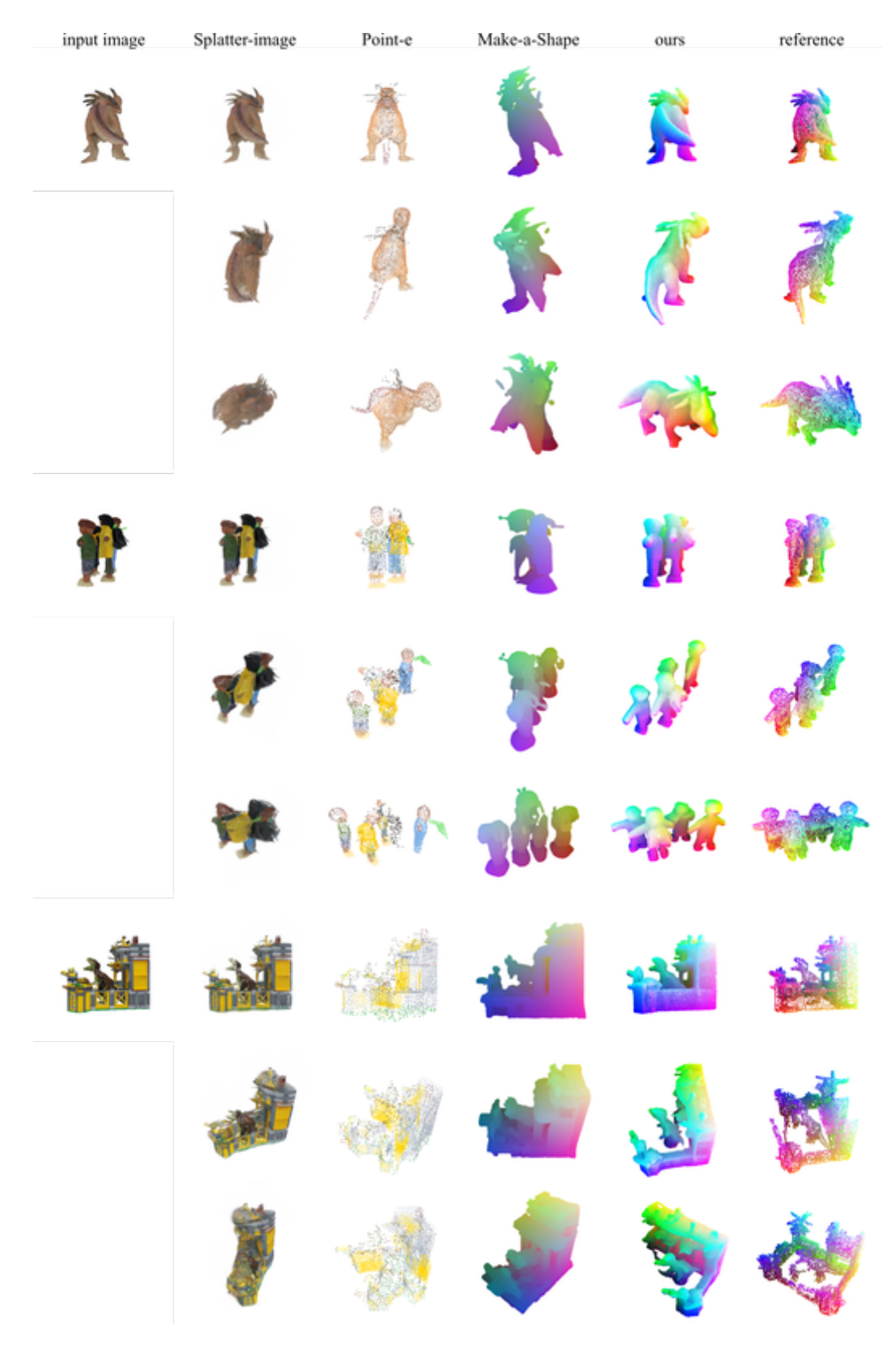


Figure 8. Single-image-to-3D results on Google Scanned Objects (1/3). Each row block shows different views of the same generated 3D representation from the same input image.

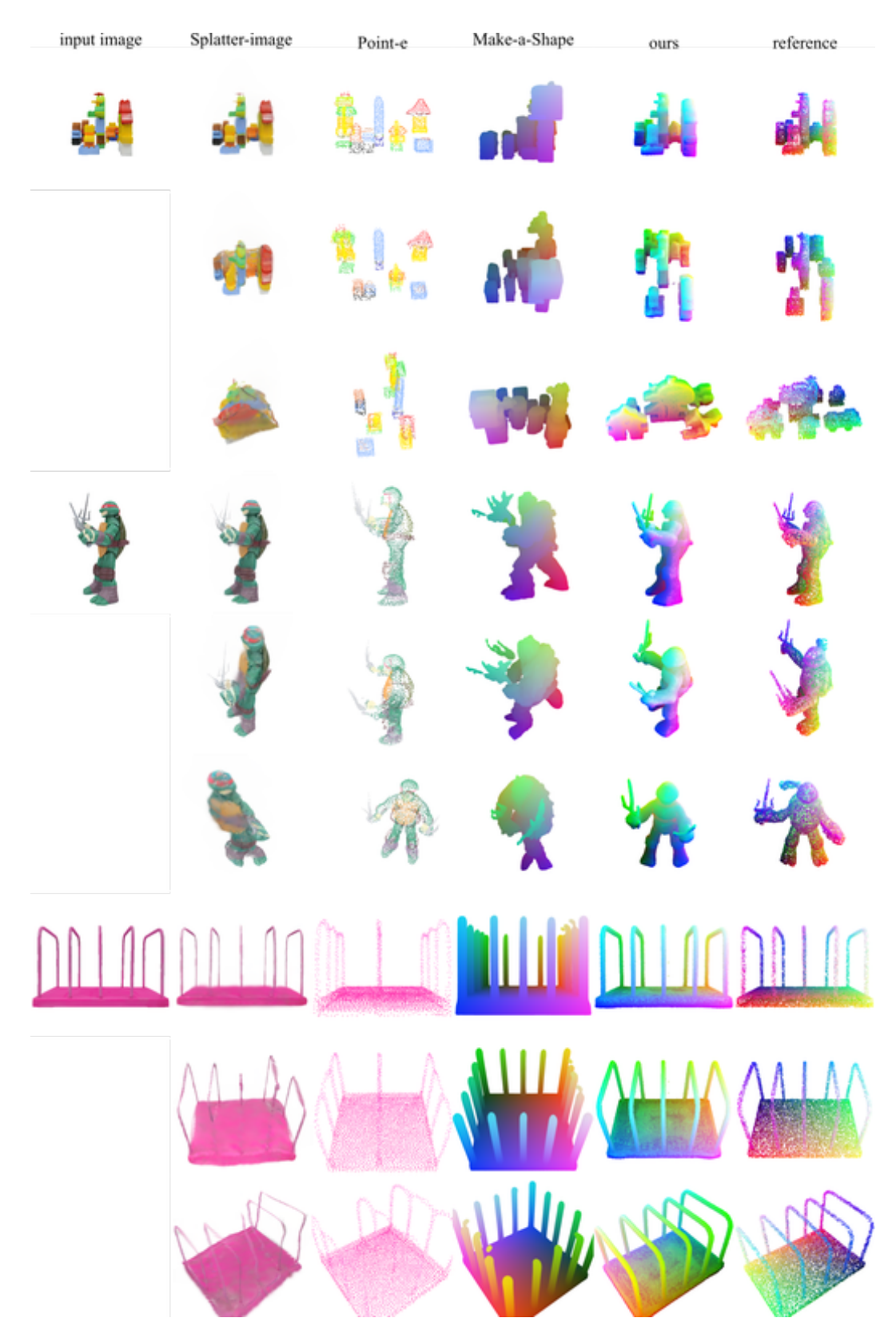


Figure 9. Single-image-to-3D results on Google Scanned Objects (2/3). Each row block shows different views of the same generated 3D representation from the same input image.

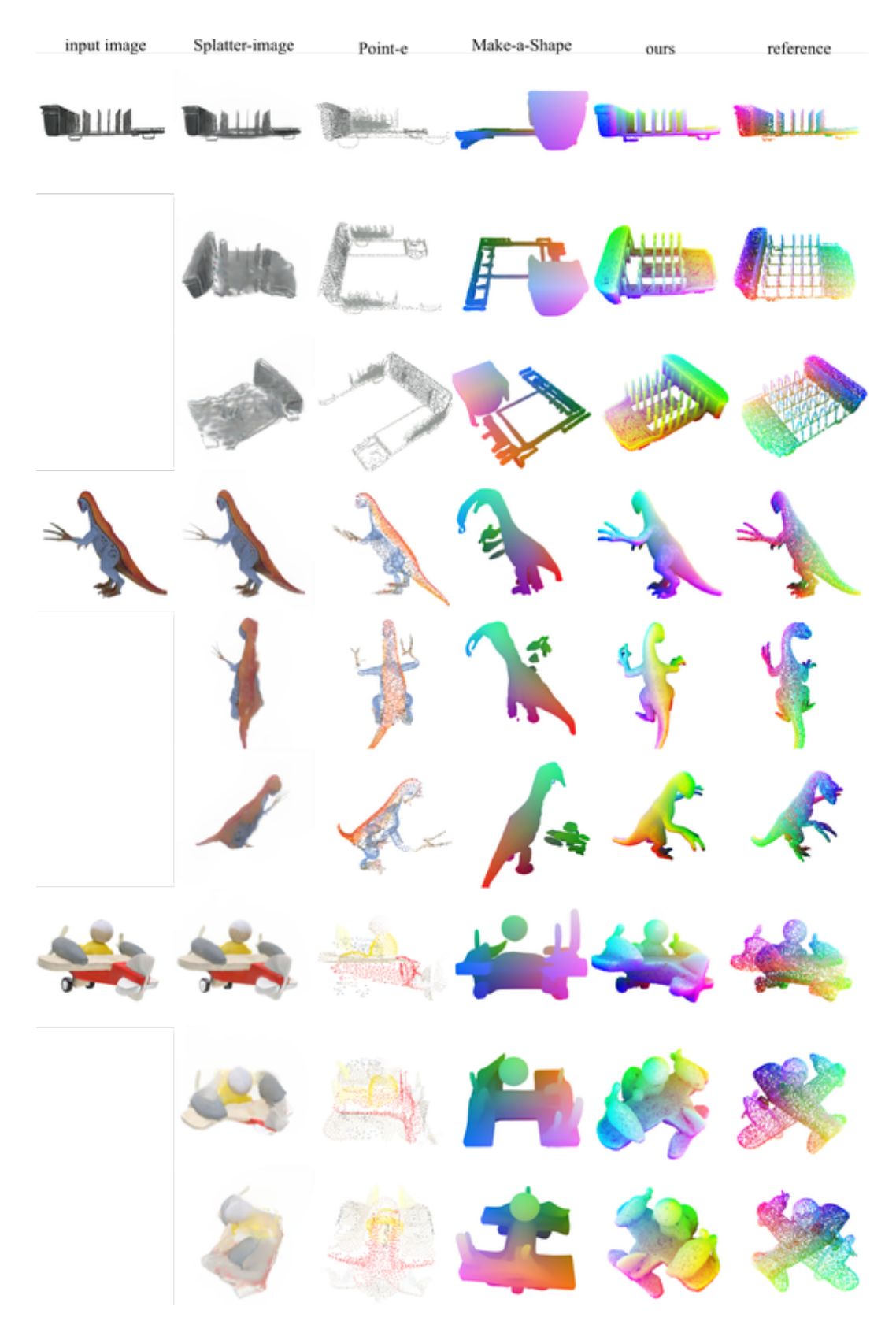


Figure 10. Single-image-to-3D results on Google Scanned Objects (3/3). Each row block shows different views of the same generated 3D representation from the same input image.

from the surfaces after the integration. We notice that we can calculate the log-likelihood of the sampled points with a small number of steps (*e.g.*, 25) and filter the sampled point cloud by thresholding the log-likelihood. As can be seen from the results in Figure 12 (*e.g.*, the center hole in the top down view), the filtering is effective and can remove points that are not removed by the standard statistical outlier removal method. In all results of the paper, we apply log-likelihood filter to remove 10% of the points with lowest log-likelihood, and then apply statistical outlier removal with neighbor size of 3 and standard deviation to be 2 [91]. We emphasize that the filtering is only conducted for visualization, all quantitative evaluations are conducted on the unfiltered point clouds.

I. Scaling experiments of single-image-to-3D

In Figure 13, we demonstrate that the Latent Flow Matching model (LFM) trained on Shape Tokens benefits from scaling, analogous to image tokenizers (e.g., SD-VAE [67]). We train LFM of various sizes: small (S), base (B), large (L), and extra-large (XL). As shown in Figure 13(a) and (b), the ULIP-I scores increase with the size of the models and dimension of the shape tokens. Our model also supports classifer-free guidance (CFG). Figure 13(c) illustrates how CFG scales affect the ULIP-I scores.

J. Architecture of Shape Tokenizer

See Figure 15 for the detailed architecture of the shape to-kenizer. The main shape tokenizer trained on Objaverse has 55.4 million trainable parameters. We use Fourier Positional embedding [78] with 32 logarithmic spaced frequencies from 2^0 to 2^12 . We change the dimension of the final linear layer to control the dimension of the Shape Tokens.

See Figure 16 for the detailed architecture of the velocity estimator paired with the shape tokenizer. We use the same Fourier Positional embedding to encode the input xyz locations as that in the shape tokenizer. We use Fourier positional embedding following by a MLP to encode flow-matching time. The Fourier positional embedding uses 16 logarithmic spaced frequencies from 2π to $2^{16}\pi$, and the MLP has 2 linear layers (64 dimension) and SiLU activation function.

We train the shape tokenizer with AdamW [49] with $\beta_1=0.9$ and $\beta_2=0.98$. No weight decay is used. We use the learning rate schedule used by Vaswani et al. [78] with a warm-up period of 4000 iterations. During the warm-up iterations, the learning rate increases to 2.8e-4, and it gradually decreases afterwards. We train the shape tokenizers on 32 H100 GPUs for 200 hours (1.2M iterations). We do not observe overfitting, since each point cloud contains a large number of i.i.d. samples of $p_{\mathcal{S}}(x)$.

The neural rendering model uses the same architecture

Table 7. Runtime (in seconds)

	H100		A1	00
	bfloat16	float32	bfloat16	float32
compute Shape Tokens	0.022	0.028	0.025	0.047
sample 16384 points from Shape Tokens with 100 Euler steps	0.72	2.81	1.18	3.58
sample shape tokens from single image with 100 Euler steps	6.76	23.12	9.20	33.56
single image to point cloud	7.48	25.93	10.38	37.14

as the flow-matching velocity estimator above. Without self-attention blocks, it processes individual rays independently. We remove the adaptive layer normalization with flow-matching time (*i.e.*, it uses standard layer normalization layers). It takes encoded ray as input and repeats the blocks 4 times. The ray is encoded as ray origin and direction. The coordinate of the ray origin is encoded with the same Fourier positional embedding as above. The direction is encoded with Plucker ray representation [62]. Additionally, we sample 32 points uniformly on the ray within the [-1, 1] box (only after the ray origin if it is within the box). We empirically find that it improves the estimation of ray hit slightly. We train the model on 32 A100 GPUs for 250 hours (880k iterations).

K. Runtime analysis

In Table 7, we report the runtime of (a) computing Shape Tokens from 16,384 input points, (b) sampling 16,384 points from Shape Tokens with 100 Euler steps, (c) sampling the image-conditioned latent flow matching model with 100 Euler steps, and (d) total time to generate a point cloud containing 16,384 points from a single image. We measure the runtime with various combinations of hardware (H100, A100) and floating point precision (bfloat16, float32). Encoding point clouds into Shape Tokens is fast (e.g., 25 ms on A100 with bfloat16), since it is a feedforward model. Sampling point clouds or Shape Tokens requires numerical integration and calling the flow matching models multiple times. Under the settings, generating a point cloud from a single image takes ¿7.5 seconds using H100 and bfloat16. There is usually a trade-off between reducing the number of steps, numerical integration method (e.g., first order, second order, etc.), runtime, and generation quality. Utilizing advancement in diffusion model speedup is future work.

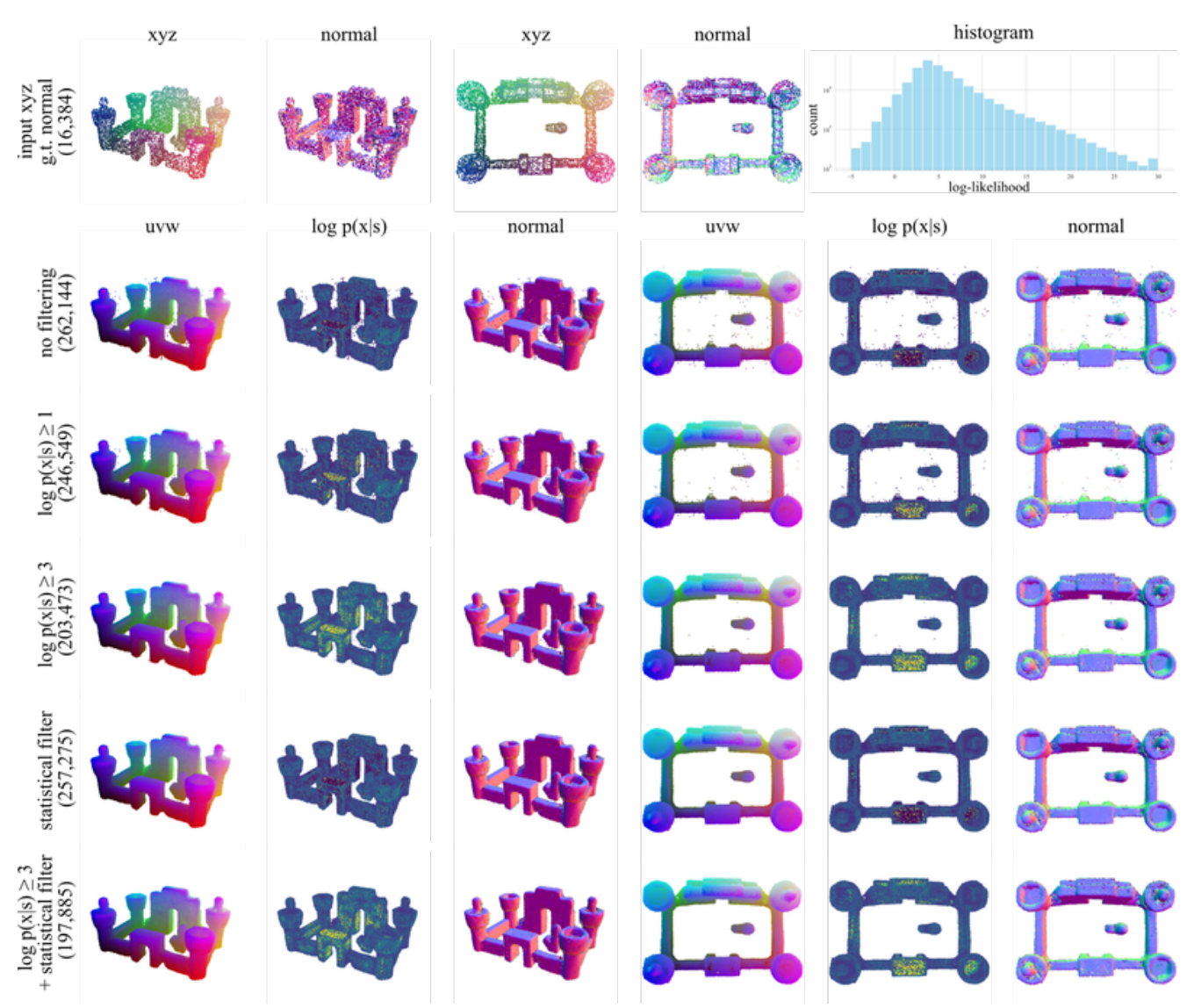


Figure 11. Denoising with log-likelihood. We sample 262k points from p(x|s). Due to error from the numerical integration, a small number of points contain noise. We compute exact log-likelihood $\log p(x|s)$ for each point and use the values to filter. Log-likelihood filtering is complementary to the standard statistical outlier filtering, which also effectively filters noisy points.

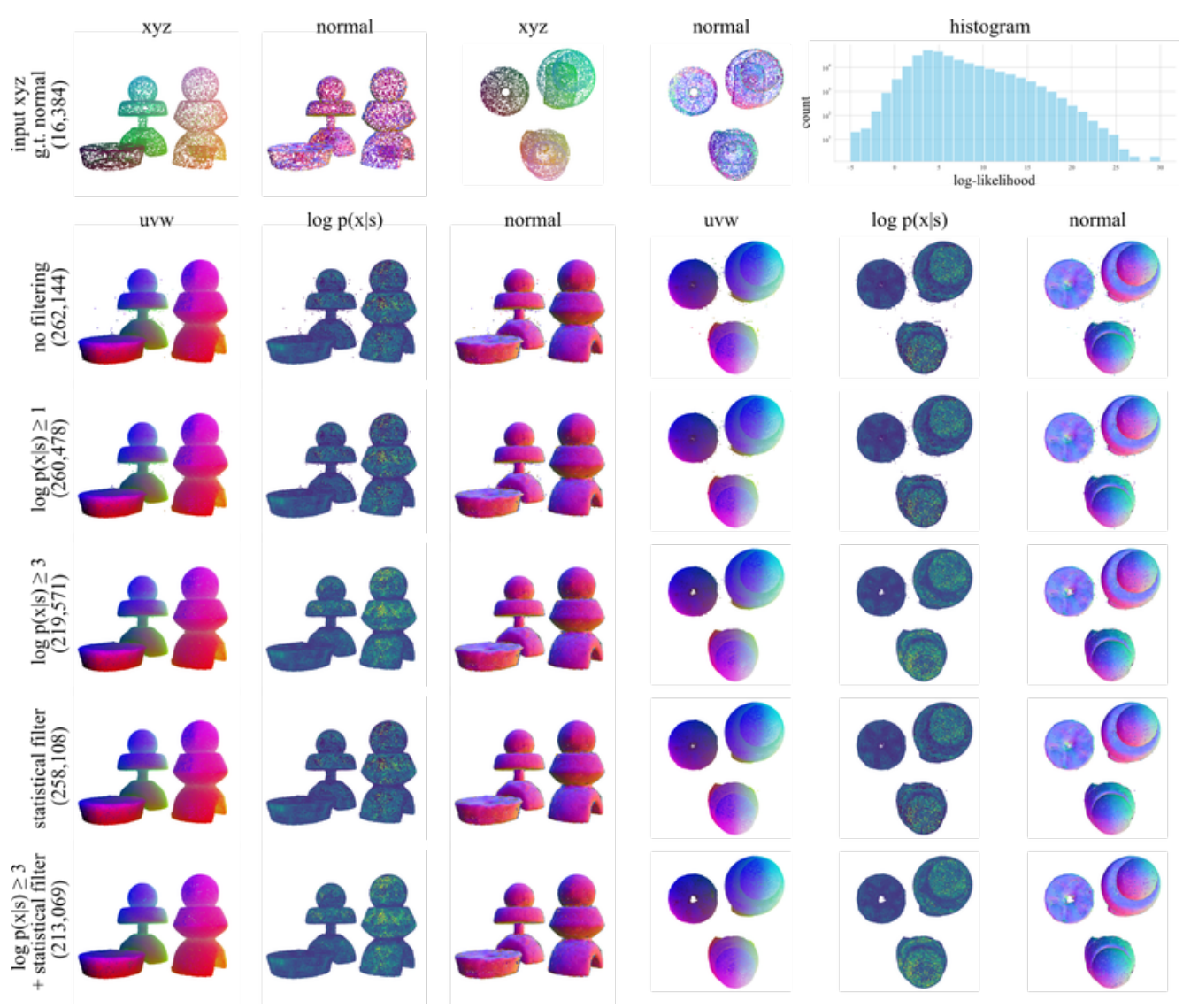


Figure 12. Denoising with log-likelihood. We sample 262k points from p(x|s). Due to the finite capacity of neural network and the large number of points, a small number of points contain noise. We compute exact log-likelihood $\log p(x|s)$ for each point and use the values to filter. Log-likelihood filtering is complementary to the standard statistical outlier filtering, which also effectively filters noisy points.

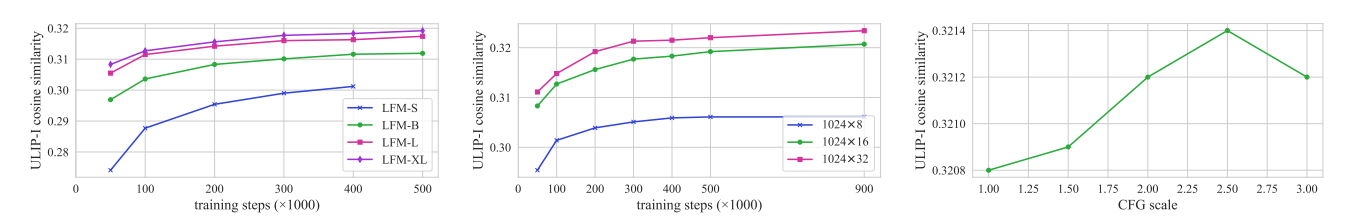


Figure 13. ULIP-I cosine similarities of (a) different model sizes, (b) different latent dimensions, and (c) different CFG scales.

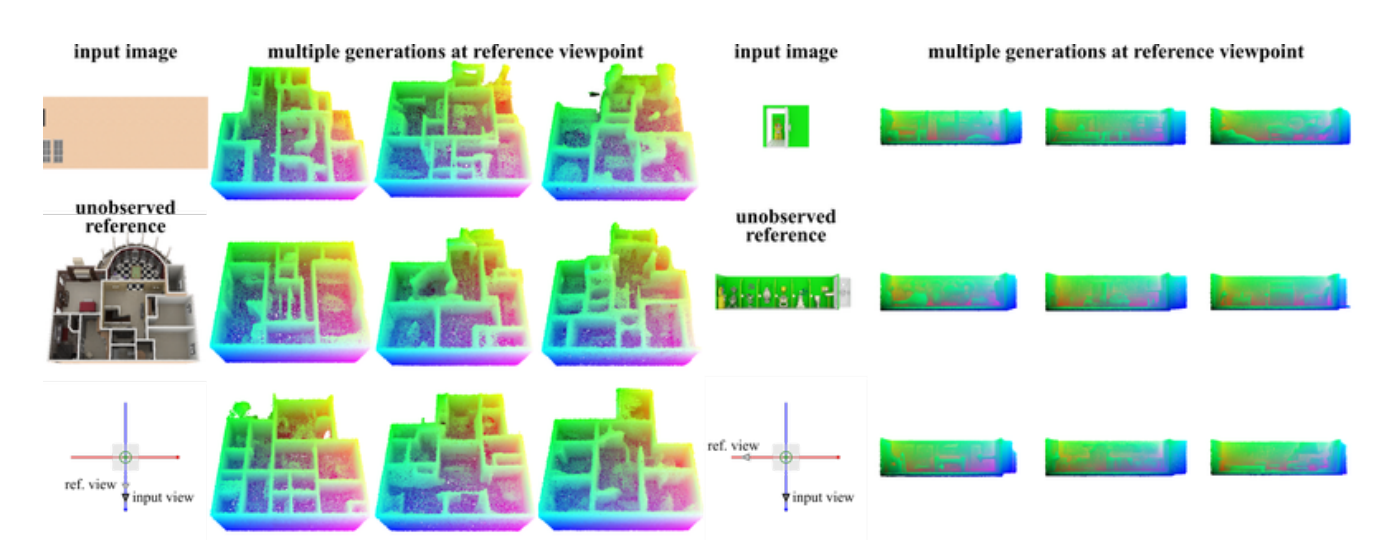


Figure 14. We generated 9 point clouds independently from the same image. We provide the rendered image of the meshes at the same viewpoint as a reference. Note that the model does not observe the reference images. Mesh credits [1, 7].

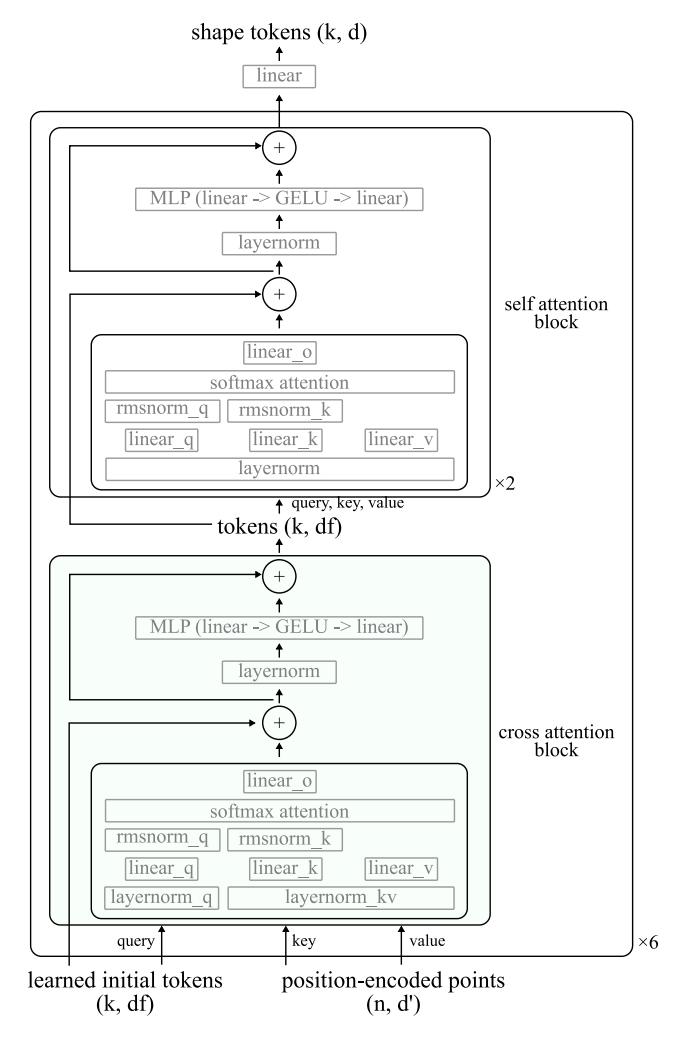


Figure 15. Architecture of shape tokenizer. Our main model for Objaverse uses $n=16,384,\ k=1024,\ df=512,\ and\ d=16.$ This results in 55.4 million trainable parameters. For shape tokenizers trained on ShapeNet, we use $n=2048,\ k=32,\ df=512,\ and\ d=64,\ resulting$ in 54.9 million trainable parameters. All multihead attention uses 8 heads. The linear layers in MLP have expand and contract the feature dimension by 4 times.

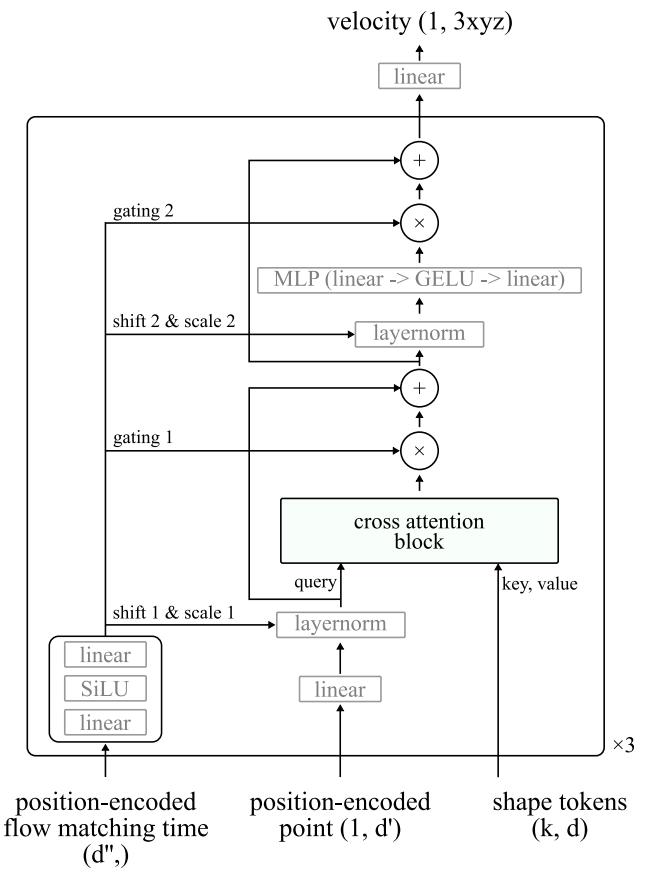


Figure 16. Architecture of flow-matching velocity estimator for shape tokenization. The model uses feature dimension 512, and the number multihead attention is 8. The linear layers in MLP have expand and contract the feature dimension by 4 times. The total number of trainable parameters is 8.72 millions and 8.87 millions for Objaverse and ShapeNet models, respectively. The neural rendering model uses the same architecture without the adaptive layer normalization with flow-matching time (*i.e.*, it uses standard layer normalization layers). It takes encoded ray as input and repeats the blocks 4 times.